AGU PUBLICATIONS

JGR

Journal of Geophysical Research: Solid Earth

RESEARCH ARTICLE

10.1002/2015JB012051

Key Points:

- Non-Dieterich-type frictional healing was observed in carbonate fault rocks
- Healing of fault-core gouges was enhanced under hydrothermal conditions
- Interseismic healing processes lead to slip stabilization of carbonate faults

Supporting Information:

- Texts S1 and S2 and Figure S1

Correspondence to:
J. Chen,
jychen@ies.ac.cn

Citation:
Chen, J., B. A. Verberne, and C. J. Spiers (2015), Effects of healing on the seismogenic potential of carbonate fault rocks: Experiments on samples from the Longmenshan Fault, Sichuan, China, *J. Geophys. Res. Solid Earth*, *120*, 5479–5506, doi:10.1002/2015JB012051.

Received 21 MAR 2015
Accepted 1 JUL 2015
Accepted article online 14 JUL 2015
Published online 28 AUG 2015

Effects of healing on the seismogenic potential of carbonate fault rocks: Experiments on samples from the Longmenshan Fault, Sichuan, China

Jianye Chen[1,2], Berend A. Verberne[2], and Christopher J. Spiers[2]

[1]State Key Laboratory of Earthquake Dynamics, Institute of Geology, China Earthquake Administration, Beijing, China, [2]HPT Laboratory, Department of Earth Sciences, Utrecht University, Utrecht, Netherlands

Abstract Fault slip and healing history may crucially affect the fault seismogenic potential in the earthquake nucleation regime. Here we report direct shear friction tests on simulated gouges derived from a carbonate fault breccia, and from a clay/carbonate fault-core gouge, retrieved from a surface exposure of the Longmenshan Fault Zone (LFZ) which hosted the 2008 Wenchuan earthquake. The experiments were conducted under dry and hydrothermal conditions, at temperatures up to 140°C, at an effective normal stress of 50 MPa, and involved sequential velocity-stepping (VS), slide-hold-slide (SHS), and velocity-stepping stages. Dry tests performed on breccia-derived samples showed no dependence of (quasi) steady state friction (μ_{ss}) on SHS or VS history, and a log linear relation between transient peak healing ($\Delta\mu_{pk}$) and hold time, or classical "Dieterich-type" healing behavior. By contrast, all experiments conducted under hydrothermal conditions were characterized by "non-Dieterich" healing behavior. This included (1) an increase in μ_{ss} upon resliding after a hold period and (2) an increase in friction rate parameter ($a - b$), after SHS testing. Comparison with previous results suggests that the healing behavior seen in our wet tests may be attributed to solution transfer processes occurring during hold periods. Our findings imply that the shallow portions of faults with carbonate/clay-rich cores (e.g., the LFZ) can heal much faster than previously recognized, while the upper limit of the seismogenic zone may migrate to deeper levels during interseismic periods. These effects have important implications for understanding the seismic cycle in tectonically active carbonate terrains.

1. Introduction

In the continental crust, most moderate-to-large earthquakes nucleate on faults at mid-to-lower crustal depths, i.e., at 10–25 km [*Sibson*, 1982; *Scholz*, 2002]. For this reason, studies of rupture nucleation and propagation have focused mainly on characterizing the frictional properties of crystalline basement rocks, such as granite, gabbro, and gouges derived from these [e.g., *Dieterich*, 1972; *Byerlee*, 1978; *Fredrich and Evans*, 1992; *Blanpied et al.*, 1995; *Marone*, 1998b; *He et al.*, 2007]. However, in tectonically active, carbonate cover terrains, destructive earthquakes often nucleate at shallower levels [e.g., *Chiarabba et al.*, 2009]. Frictional sliding experiments conducted on simulated calcite(-rich) fault gouges at upper crustal conditions have revealed that these materials are both strong (friction coefficient of ~0.7) and prone to velocity-weakening slip at relatively low temperatures (as low as 80°C) [*Drennon and Handy*, 1972; *Olsson*, 1974; *Weeks and Tullis*, 1985; *Verberne et al.*, 2013a]. This is consistent with the shallow seismicity and shallow upper limit of the seismogenic zone seen in carbonate cover regions [e.g., *Bernard et al.*, 2006; *Chiarabba et al.*, 2009]. Destructive earthquakes occurring in such terrains include the 1995 M_w 6.2 Aigion earthquake in Greece (hypocentral depth 7.2 km [*Bernard et al.*, 2006]); the 2009 M_w 6.3 L'Aquila earthquake in Italy (9.5 km [*Chiarabba et al.*, 2009]); and the 2008 M_w 7.9 Wenchuan earthquake in Sichuan, China (<10 km in the northern segment [*Zhao et al.*, 2010]). Despite such events, though, very few data are available on the frictional and healing behavior of carbonate fault rocks, and to improve seismic hazard assessment in carbonate terrains, a much better understanding of the frictional properties of natural carbonate fault rocks is needed [e.g., *Scuderi et al.*, 2013; *Carpenter et al.*, 2014].

Most of the frictional experiments that have been done on carbonate rocks to date were performed at coseismic slip rates [e.g., *Han et al.*, 2007]. Only a few studies have addressed the rate-and-state friction (RSF) behavior in the seismic nucleation regime or the underlying microphysical mechanism(s) that lead to stable (aseismic) versus unstable (seismogenic) slip [*Weeks and Tullis*, 1985; *Verberne*, 2010; *Scuderi et al.*, 2013]. Even fewer studies have addressed carbonate fault healing and associated strength recovery, although these aspects have been widely studied in relation to both natural [*Li et al*., 2003; *Marone et al*., 1995] and laboratory faults [*Wong and Zhao*, 1990; *Karner and Marone*, 2001] in silicate rocks, as they strongly affect earthquake nucleation, magnitude, and recurrence intervals [e.g., *Ruina*, 1983; *Marone*, 1998a].

Moreover, while numerous studies have investigated the effects of mineral and fluid compositions, environmental conditions, and fault displacement on the slip-rate dependence of friction in silicate rocks (see reviews by *Marone* [1998a] and by *Paterson and Wong* [2005]), we are aware of no work experimentally addressing how the velocity dependence of friction in either silicates or carbonates evolves with time, especially in (static) interseismic periods. In both experiment and nature, carbonate rocks are well known to exhibit ductile deformation by mechanisms such as crystal plasticity and pressure solution, at lower pressures and temperatures than generally required for similar mechanisms to operate in silicate-dominated crustal rocks [e.g., *Liu et al*., 2002]. At seismogenic depths, where these thermally activated and (or) fluid-assisted deformation mechanisms are expected to operate, faults heal during interseismic periods, as the internal microstructural state of the gouge changes [e.g., *Yasuhara et al*., 2005; *Niemeijer et al*., 2008]. However, how healing by these processes may affect the velocity dependence of fault friction is virtually unexplored.

Lastly, the effects of phyllosilicates on the frictional and healing properties of carbonate fault rocks need to be considered. Phyllosilicate-rich fault rocks have long attracted attention [*Morrow et al*., 1992; *Tembe et al*., 2010; *Carpenter et al*., 2012; *Den Hartog et al*., 2013], due to their widespread occurrence and role in controlling the dynamics of rupture nucleation and propagation at shallow crustal levels [e.g., *Tesei et al*., 2012]. It is well known that the presence of phyllosilicates, such as smectite, in fault zones may significantly reduce fault frictional strength [e.g., *Tembe et al*., 2010] as well as rates of interseismic fault restrengthening [*Bos and Spiers*, 2002; *Carpenter et al*., 2012]. Moreover, recent studies of faults, such as that hosting the 2008 M_w 7.9 Wenchuan earthquake [*Hou et al*., 2012; *Chen et al*., 2013a], have revealed that clay mineral content can become strongly enriched in carbonate fault cores at relatively shallow depth [see also *Bullock et al*., 2014; *Viti et al*., 2014], due to extensive rock-fluid interaction [e.g., *Chen et al*., 2013a]. This raises the question of how clay minerals influence the frictional and healing behavior of clay/carbonate fault core rocks under in situ hydrothermal conditions.

In this paper, we expand on previous preliminary experiments [*Chen et al*., 2015], with the aim of determining the rate dependence of friction, and the effects of healing upon this, in both dry and wet carbonate fault rocks subjected to direct shear at 0.1–10 μm/s, at 20 to 140°C, and at 50 MPa effective normal stress. The samples used were derived from both immature carbonate breccia and clay-rich fault core gouge collected from a surface exposure of the Wenchuan earthquake rupture, Sichuan, China. Our results show marked healing and history-related slip stabilization effects in the presence of water. We consider the microphysical mechanisms responsible for the observed behavior as well as the implications of our results for fault slip, slip stabilization, and interseismic strength recovery in tectonically active carbonate terrains in general.

2. Materials and Methods

2.1. Sample Materials

We collected samples from a surface exposure of the Yingxiu-Beichuan Fault (YBF), a principal branch of the Longmenshan Fault Zone (LFZ), which hosted the 2008 M_w 7.9 Wenchuan earthquake. A 240 km long surface rupture was generated during the earthquake [*Xu et al*., 2009], with the largest displacement of ~11 m occurring on the YBF some 3 km from our sampling site [*P. Zhang et al*., 2010; *Chen et al*., 2013a]. At the exposure studied, the coseismic rupture cuts through extensive carbonate strata, reactivating an ~5 m wide fault zone with a typical breccia-gouge-breccia sandwich structure [*Mizoguchi et al*., 2008; *Hou et al*., 2012; *Chen et al*., 2013a] and producing a vertical displacement of ~6.5 m [*Xu et al*., 2009]. The width of the fault core is relatively narrow, with a 2 cm thick gouge developed in the center, representing the only principal slip zone that can be found within the fault. Mineralogical analysis revealed increasing enrichment in clay toward the slip zone, from ~2% at the margin to 35% in the fault gouge. A detailed description of the exposure and relevant fault rocks is given by *Chen et al*. [2013b].

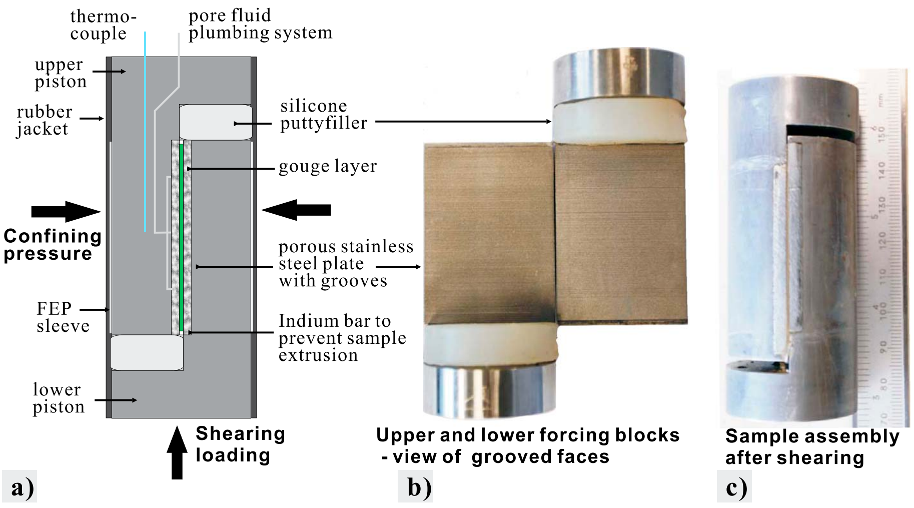

Figure 1. Sample assembly used for the present direct shear experiments performed in a triaxial deformation apparatus. (a) Cross section of the sample assembly. (b) Upper and lower 69 shearing blocks with grooved plates of porous stainless steel. (c) Sample assembly after deformation, with extruded silicone putty filler removed.

In the experiments reported here, a clay-rich gouge sample and a typical (clay-poor) breccia sample were chosen as starting materials. X-ray diffraction analyses revealed that the fault breccia mainly consists of calcite (68%) and dolomite (29%), with minor clay (2%) and quartz (1%). The fault gouge consists of clays (35%, smectite-illite and chlorite), quartz (29%), dolomite (27%), and calcite (7%), with minor feldspar (2%). Simulated fault gouges were produced from both materials by crushing and sieving to produce powders with a grain size (sieve mesh) less than 35 μm. The breccia sample was chosen in order to obtain a simulated gouge with a chemically unaltered fault rock composition, appropriate for studying (recurrent) rupture nucleation at depth, while the gouge sample was used to represent the fault core material developed in the shallow portion of the fault zone [*Chen et al.*, 2013a]. Where context leaves no ambiguity, the term “gouge” will be used in this paper to cover both simulated and natural gouges.

2.2. Experimental Apparatus and Direct Shear Sample Assembly

All experiments were performed on 1 mm layers of the above-mentioned gouges, sandwiched in a direct-shear sample assembly located within a conventional triaxial testing apparatus. The triaxial machine comprised a pressure vessel and pressure-balanced axial loading piston [*Verberne et al.*, 2013b]. Confining pressure (P_c) was applied using an external diaphragm pump, and held constant to within ~0.1 MPa of the desired test value, using a servo-controlled volumetric pump. An internal force gauge was used for measurement of axial force independently of seal friction. In wet experiments, pore pressure was applied and controlled using a high-precision, volumetric servo pump. During individual wet experiments, pore fluid volume changes determined using this system were used as a measure of sample compaction or dilatation normal to the shear plane. In experiments at elevated temperature, heating was achieved using a Thermocoax internal furnace. Sample temperature was measured using a thermocouple located within the direct shear assembly, close to the sample (Figure 1a). Temperature fluctuations varied within ±2.0°C during each experiment.

The direct shear assembly used in the experiments consisted of a “69” or direct shear forcing block set specially designed for use in triaxial testing machines (Figure 1). For a detailed description, see *Samuelson and Spiers* [2012]. The setup consists of two, opposing, direct shearing blocks, each comprising a half cylinder with a full cylindrical base at one end (diameter 35 mm). Besides being easily jacketable, this geometry has the advantage that the normal stress acting on the gouge layer, sandwiched between two shear blocks (Figure 1a), is independent of shear displacement and is equal to the applied P_c at all times. Internal pore fluid plumbing provides fluid access to the shearing surface of each half cylinder, which consists of a grooved plate of porous (sintered) stainless steel (Figure 1a). These plates provide traction to the sample and ensure even access of pore fluid to the sample surfaces (Figure 1b). The grooves are spark-eroded into the porous plates at a spacing of 100 μm, being 120 μm wide and 60 μm deep (Figure 1b).

In preparing each experiment, we mixed ~4.5 g of sample powder with ~1.5 mL sample-saturated demineralized water to yield a moldable paste. A specially designed jig allowed for easy emplacement of a 1 mm (±0.05 mm) thick layer of this gouge paste onto the grooved/porous surface of one of the direct shear blocks. Initial layer dimensions measured 49 mm in length by 35 mm in width. For dry experiments, the sample assembly was dried in an oven at ~105°C for at least 3 h to remove the added water. To avoid extrusion of sample material upon shear deformation, 1 mm sections of the sample layer length were removed from the ends of the layer, using a razor blade, and replaced by two soft indium bars measuring 1 × 1 × 35 mm. In this way, a 47 × 35 × 1 mm plate of gouge paste was left, onto which the second shear block was placed (Figures 1a and 1c). The displacement-accommodating voids (9 mm long) at the ends of the gouge layer were then plugged with silicone putty enveloped in PTFE foil (Figure 1b). These plugs "flow" in response to axial shortening of the assembly, accommodating the imposed displacement with undetectable shear resistance (Figure 1c). Finally, the entire assembly was jacketed, first in a thin FEP heat shrink tube and then using an EPDM rubber sleeve of ~1.4 mm thickness, sealing the latter against the upper and lower shearing blocks with wire tourniquets.

2.3. Experimental Procedure

In performing each experiment, the jacketed assembly was first loaded into the pressure vessel and externally pressurized to a P_c value of ~8 MPa. For runs at elevated temperature, we then switched on the furnace and waited for at least 6 h until a near-constant sample temperature was achieved. Sample temperatures of 20, 80, and 140°C were employed. As the sample temperature approached the target value, the confining pressure, P_c, also increased. This was manually maintained below the test value until thermal equilibrium was reached, at which point servo control of the confining pressure was enabled. Wet experiments were conducted using a P_c of 65 MPa, while for dry tests we used 50 MPa. In the case of wet experiments, the pore fluid system was charged by evacuating for ~15 min, then injecting demineralized water under vacuum. The fluid was subsequently pressurized to a constant value of 15 MPa using the high-precision volumetric servo pump.

After full *P-T* equilibration, each experiment was initiated by advancing the loading piston at a constant displacement rate of 1 or 10 μm/s. After reaching steady state, we conducted, in this order, a "velocity-stepping" sequence, a "slide-hold-slide" sequence, and a second velocity-stepping sequence. The velocity-stepping sequences (VS-seq1 and VS-seq2) involved switching the load point velocity between 0.1, 1, and 10 μm/s in 5–6 steps, while the slide-hold-slide sequence (SHS-seq) consisted of 6–9 individual SHS events performed using a single velocity of 0.1, 1, or 10 μm/s per experiment. Each SHS event involved imposing the chosen sliding velocity (V_{SHS}) until a displacement of 0.2–0.5 mm was achieved, followed by a hold period of 35 s to 65.5 h duration, and then by reshearing at the same velocity (V_{SHS}). The hold times (t_h) used were typically increased from 35 s to a maximum of 2.35×10^5 s (65.5 h), in jumps of roughly 0.5 order of magnitude (~ factor of 3).

All experiments performed are listed in Table 1. They fall into four sets. Three of these correspond to experiments performed on samples prepared from wet fault gouge (Data Set 1), dry fault breccia (Data Set 2), and wet fault breccia (Data Set 3). We did not conduct experiments on "dry" fault gouge because the smectite components would assume an unknown hydration state during sample assembly and testing [cf. *De Jong et al.*, 2014], rendering comparison with wet (water-buffered) behavior of little value. In each of the above sets of experiments, we systematically varied the experimental temperature ($T = \sim 20$, 80, and140°C) and the reloading velocity employed in the SHS sequences ($V_{SHS} = 0.1$, 1, and 10 μm/s). Note that, in a few runs, only VS or SHS testing was performed, in the latter case with hold times first increasing and then decreasing (Runs 2 and 4, Table 1). One test (Run 11) was performed using a single hold period (9 h), for comparison with the multihold experiments. One test (Run 17) employed velocity stepping only but with large total displacement. Another test was run using a random hold time sequence (Run 9). This was done to investigate the effect of slip/hold history on frictional healing.

Besides the three sets of experiments addressed above, we conducted a fourth set of control experiments, in which the composition of the pore fluid was varied to gain insight into the nature of fluid-rock interactions occurring (Table 1). In three of these experiments, we used NaH_2PO_4 solution (0.01 M) as pore fluid. The

Table 1. List of Experiments, Conditions, and Key Results[a]

Experiment	T	P_c	P_f	Pore Fluid	V_{SHS}	μ_{max}	W_f	Testing Type	Healing Type	
Data Set 1: Wet gouge-derived samples										
Run 31	20	65	15	sat. water	0.1	0.310	0.75	VS-SHS-VS	Type 3	
Run 27	20	65	15	sat. water	1	0.308	0.65	VS-SHS-VS	Type 1a	
Run 25	20	65	15	sat. water	10	0.309	0.80	VS-SHS-VS	Type 3	
Run 29	80	65	15	sat. water	0.1	0.296	0.60	VS-SHS-VS	Type 2	
Run 26	80	65	15	sat. water	1	0.322	0.75	VS-SHS-VS	Type 2	
Run 30	80	65	15	sat. water	10	0.303	0.65	VS-SHS-VS	Type 2	
Run 32	140	65	15	sat. water	0.1	0.337	0.50	VS-SHS-VS	Type 2	
Run 28	140	65	15	sat. water	1	0.310	0.55	VS-SHS-VS	Type 2	
Run 33	140	65	15	sat. water	10	0.330	0.50	VS-SHS-VS	Type 2	
Average						0.314	0.64			
Data Set 2: Dry breccia-derived samples										
Run 15	20	50	atm	lab air	0.1	0.652	0.80	VS-SHS-VS	Type 1a	
Run 14	20	50	atm	lab air	1	0.65	0.83	VS-SHS-VS	Type 1a	
Run 3	20	50	atm	lab air	10	0.68	0.75	VS-SHS-VS	Type 1a/3	
Run 23	80	50	atm	lab air	0.1	0.70	0.85	VS-SHS-VS	Type 1a	
Run 19	80	50	atm	lab air	1	0.698	0.85	VS-SHS-VS	Type 1a	
Run 16	80	50	atm	lab air	10	0.691	0.95	VS-SHS-VS	Type 1a	
Run 1	140	50	atm	lab air	0.1	0.721	0.90	VS	Type 1a	b
Run 20	140	50	atm	lab air	1	0.71	0.88	VS-SHS-VS	Type 1a	
Run 18	140	50	atm	lab air	10	0.693	0.85	VS-SHS-VS	Type 1a	
Average						0.688	0.85			
Data Set 3: Wet breccia-derived samples										
Run 5	20	65	15	sat. water	0.1	0.635	0.70	VS-SHS-VS	Type 1a	
Run 12	20	65	15	sat. water	1	0.667	0.75	VS-SHS-VS	Type 1a	
Run 2	20	65	15	sat. water	10	0.66	0.65	SHS(increasing/decreasing)	Type 1a	c
Run 8	80	65	15	sat. water	0.1	0.67	0.65	VS-SHS-VS	Type 2	
Run 6	80	65	15	sat. water	1	0.67	0.70	VS-SHS-VS	Type 2	
Run 11	80	65	15	sat. water	1	0.664	0.67	VS-H-VS	Type 2	d
Run 4	80	65	15	sat. water	10	0.68	0.78	SHS(increasing/decreasing)	Type 2	c
Run 17	80	65	15	sat. water		0.67	0.70	VS		e
Run 10	140	65	15	sat. water	0.1	0.65	0.65	VS-SHS-VS	Type 2	
Run 22	140	65	15	sat. water	1	0.682	0.70	VS-SHS-VS	Type 2	
Run 9	140	65	15	sat. water	1	0.695	0.58	VS-SHS-VS	Type 2	f
Run 7	140	65	15	sat. water	10	0.69	0.72	VS-SHS-VS	Type 2	
Average						0.669	0.69			
Data Set 4: Control experiments on breccia-derived samples										
Run 37	20	65	15	phos. sol.	1	0.708	0.80	VS-SHS-VS	Type 2	g
Run 34	80	65	15	phos. sol.	1	0.672	0.75	VS-SHS-VS	Type 2	g
Run 35	140	65	15	phos. sol.	1	0.628	0.78	VS-SHS-VS	Type 2	g
Run 47	20	50	atm	silicone	1	0.715	0.85	VS-SHS-VS	Type 1a	h
Run 44	80	50	atm	silicone	1	0.705	0.85	VS-SHS-VS	Type 1a	h
Run 46	140	50	atm	silicone	1	0.720	0.85	VS-SHS-VS	Type 1a	h
Run 13	80	50	atm	sat. water	1	0.645	0.70	VS-SHS-VS	Type 2	i

[a] Abbreviations: T = temperature (°C); P_c = confining pressure (MPa); P_f = pore fluid pressure (MPa); V_{SHS} = load point velocity used during SHS stages (μm/s); μ_{max} = peak strength of material picked from the friction-displacement curves at a slip rate of 10 μm/s (interpolated where necessary); W_f = final thickness of the gouge layer (mm); VS = velocity stepping; SHS = slide-hold-slide; atm = atmospheric pressure; phos. sol. = phosphate solution; sat. water = sample-saturated demineralized water.

[b] Occurrence of marked stick slips at all sliding velocities used. Velocity-stepping sequence only.

[c] SHS tests only, in which the hold times used were first applied in a forward (increasing) sequence and then in the reverse (decreasing) sequence.

[d] A run, in which the SHS sequence contained one hold period (9 h) only. This procedure is accordingly referred to as "VS-H-VS."

[e] A run with VS-seq only, stepping between 1 and 10 μm/s, over a relatively large displacement interval.

[f] A run performed using random hold times (35 s-100 s-300 s-900 s-54,960 s-2700 s-6600 s-18,000 s).

[g] Experiments using 0.01 M NaH_2PO_4 solution as pore fluid.

[h] Experiments using silicon oil as pore fluid.

[i] An experiment using a water-saturated sample drained to the atmosphere, i.e., tested wet at zero pore fluid pressure.

presence of phosphate ions in solution is known to slow down the rate of intergranular pressure solution creep [e.g., *X. Zhang, et al.*, 2010]. In a second set of three experiments, we used silicone oil as a chemically inert fluid. Finally, to test the effect of pore pressure on our wet experiments, an additional experiment was performed on a water-saturated sample drained to atmospheric conditions. In all experiments employing an aqueous pore fluid, since the gouge samples used were fine grained and the time between fluid injection and test initiation were typically 8 h, we assume that the pore fluid was close to being saturated with the soluble components of the samples.

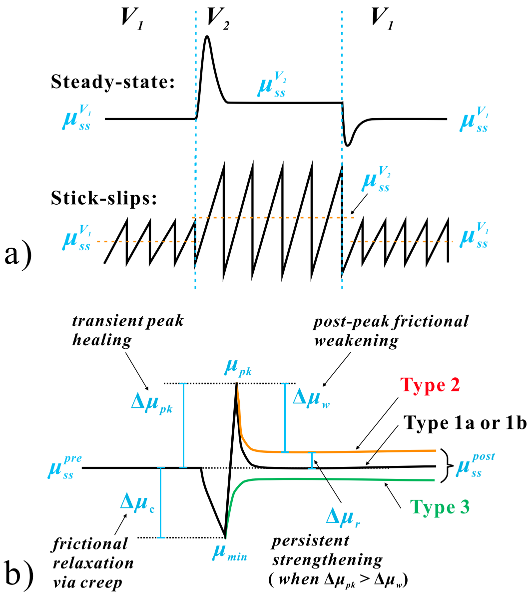

Figure 2. Methods for determining the frictional and healing parameters from velocity-stepping and slide-hold-slide data in our experiments. (a) Terminology for describing the "steady state" friction coefficient measured in velocity-stepping tests, in the cases of stable sliding and stick-slip behavior. Friction rate parameter $(a - b) = (\mu_{ss}{}^{V2} - \mu_{ss}{}^{V1})/\ln(V_2/V_1)$. (b) Definition of frictional healing parameters and classification of healing behavior after *Chen et al.* [2015]. Note that Type 1 behavior can be further divided into Type 1a (classical Dieterich type, characterized by log linear relation between $\Delta\mu_{pk}$ and hold time) and Type 1b (any other relationship).

2.4. Data Processing

For each experiment, we calculated the apparent friction coefficient (μ) by taking the ratio of shear stress to effective normal stress supported by the gouge layer, thus including contribution by cohesion. Using the friction versus displacement data obtained in the VS-seqs and SHS-seqs, we then obtained the frictional rate dependence and healing parameters as follows. Note that the measured displacement was corrected for elastic machine distortion using calibrations obtained from compression tests on a steel dummy of known elastic properties.

Starting with the VS data, we used the (quasi) steady state frictional strength (μ_{ss}) reached before and after each velocity step (V step) to determine the RSF rate dependence parameter, $(a - b) = \Delta\mu_{ss}/\Delta\ln V = (\mu_{ss}{}^{V2} - \mu_{ss}{}^{V1})/\ln(V_2/V_1)$ [*Marone*, 1998a] (Figure 2a). In the case of unstable stick slips, we took the average strengths at the relevant sliding velocities to obtain apparent $(a - b)$ values (Figure 2a). We determined $(a - b)$ for all V steps in the range of 0.1–1 μm/s and 1–10 μm/s. Recall that in the framework of rate-and-state-dependent friction theory, positive values of $(a - b)$ indicate intrinsically stable, velocity-strengthening behavior, whereas negative values indicate potentially unstable, velocity-weakening behavior, which is prerequisite for unstable stick-slip behavior [*Ruina*, 1983; *Scholz*, 2002].

For each SHS sequence and constituent SHS event, we quantified (1) the magnitude of stress relaxation and (2) the magnitude of frictional healing obtained after each hold period. In the conventional methodology for SHS data processing [e.g., *Marone*, 1998a], the magnitude of frictional relaxation ($\Delta\mu_c$) due to creep effects during the hold period is defined as the difference between μ_{ss}^{pre} and the minimum frictional strength (μ_{min}) attained during relaxation (Figure 2b). The magnitude of frictional healing achieved after a hold time is defined as the difference between the steady state friction measured before or after the hold period ($\mu_{ss}^{\text{pre}} = \mu_{ss}^{\text{post}}$) and the peak frictional strength associated with reshearing (μ_{pk}). However, in some of our experiments, we observed marked changes in the prehold and posthold steady state friction coefficients, μ_{ss}^{pre} versus μ_{ss}^{post}, across individual hold periods (Figure 3). This kind of behavior has been reported in some previous studies [e.g., *Nakatani and Mochizuki*, 1996] and is not easily described using the conventional notation of *Marone* [1998a]. Therefore, following the method recently developed by *Chen et al.* [2015], we use three parameters to describe frictional healing behavior—see Figure 2b. In this scheme, $\Delta\mu_{pk}$ is the transient peak healing, measured in terms of the difference ($\mu_{pk} - \mu_{ss}^{\text{pre}}$), which corresponds to the "healing" (termed $\Delta\mu$) specified in the conventional definition [e.g., *Marone*, 1998a]. By contrast, $\Delta\mu_w$ is the postpeak frictional weakening, measured as the difference ($\mu_{pk} - \mu_{ss}^{\text{post}}$), and $\Delta\mu_r$ is the residual, persistent strengthening effect, measured as the difference ($\mu_{ss}^{\text{post}} - \mu_{ss}^{\text{pre}}$). Using these parameters,

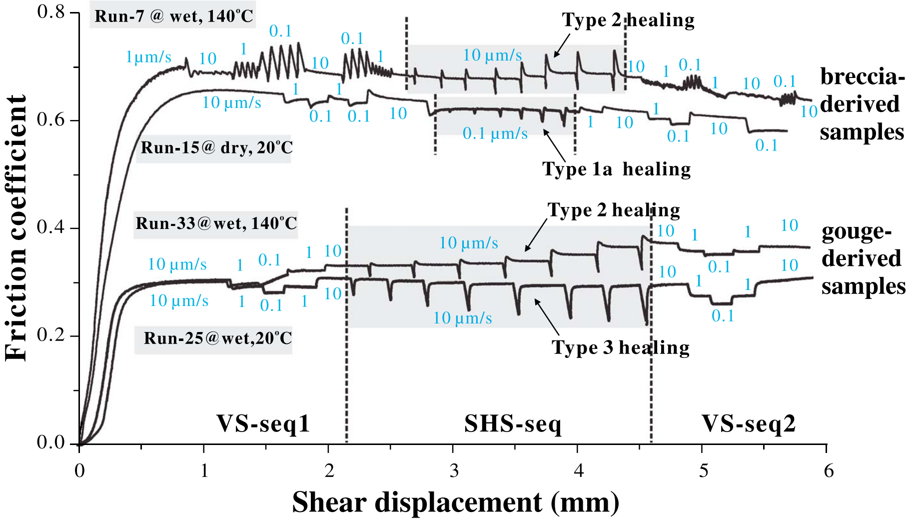

Figure 3. Representative friction versus displacement curves obtained from shearing experiments performed on powdered samples derived from carbonate-clay fault gouge and carbonate fault breccia. After a "run-in" at constant velocity, velocity-stepping (VS) tests were employed to evaluate the rate dependence of frictional strength (VS-seq1). This was followed by a slide-hold-slide testing sequence (SHS-seq) and finally a second VS sequence (VS-seq2). Effective normal stress was 50 MPa in all cases. Wet experiments were performed at a confining pressure of 65 MPa and a pore pressure of 15 MPa.

and taking into account the way they depend on hold time, this scheme allows definition of all possible categories of frictional healing behavior. Note that a few of the present experiments exhibited minor, near-linear slip hardening or weakening behavior in some of the velocity intervals employed in the VS and SHS stages of the tests. These effects were corrected using noncumulative linear detrending of the data, following the approach introduced by *Blanpied et al*. [1995] [see also *Verberne et al*., 2013b].

Lastly, compaction of the gouge layer in experiments on wet breccia-derived samples was estimated by dividing the pore fluid volume change, obtained from the volumetric pump, by the area of the gouge layer. This yielded thickness change versus time data for the entire duration of each wet experiment, from which the compaction strain rate ($\dot{\varepsilon}$) was further calculated. Error analyses pertaining to the frictional parameters and compaction data presented in this study are given in Text S1 in the supporting information. We do not report compaction data for the gouge-derived samples because the resolution of the data obtained was not high enough, due to a later-discovered recording problem in these experiments. In addition, ongoing shear deformation occurring during relaxation in "static" hold periods allowed us to determine shear strain rate ($\dot{\gamma}$) versus hold time from the stress relaxation data. The approach used for this followed the classical method applied by *Rutter and Mainprice* [1978]. By comparing the results at different temperatures, activation energies for the operative compaction and relaxation creep processes were obtained by plotting ln $\dot{\varepsilon}$ or ln $\dot{\gamma}$ against 1/*T* (see Text S2).

3. Experimental Results

3.1. Representative Results and General Features

Representative plots of frictional strength versus shear displacement for both the fault-gouge-derived and fault-breccia-derived samples are presented in Figure 3. Henceforth, we will refer to the two materials simply as gouge derived and breccia derived. All samples tested showed a rapid increase in friction coefficient in the first 0.3 to 0.5 mm of displacement, followed by macroscopic yield and gradual hardening toward an apparent peak value attained at around 1.0 mm of displacement. The frictional strength subsequently increased or decreased slightly in the VS-seq1, SHS-seq, and VS-seq2 stages of each experiment, depending on imposed sliding velocity and/or hold time. A cumulative displacement of 5–6 mm was achieved in each test.

Generally speaking, peak friction values (μ_{max}), picked at ~1 mm displacement at a slip rate of 10 μm/s to roughly characterize the strength of the material, ranged from 0.30 to 0.34 for the gouge-derived samples

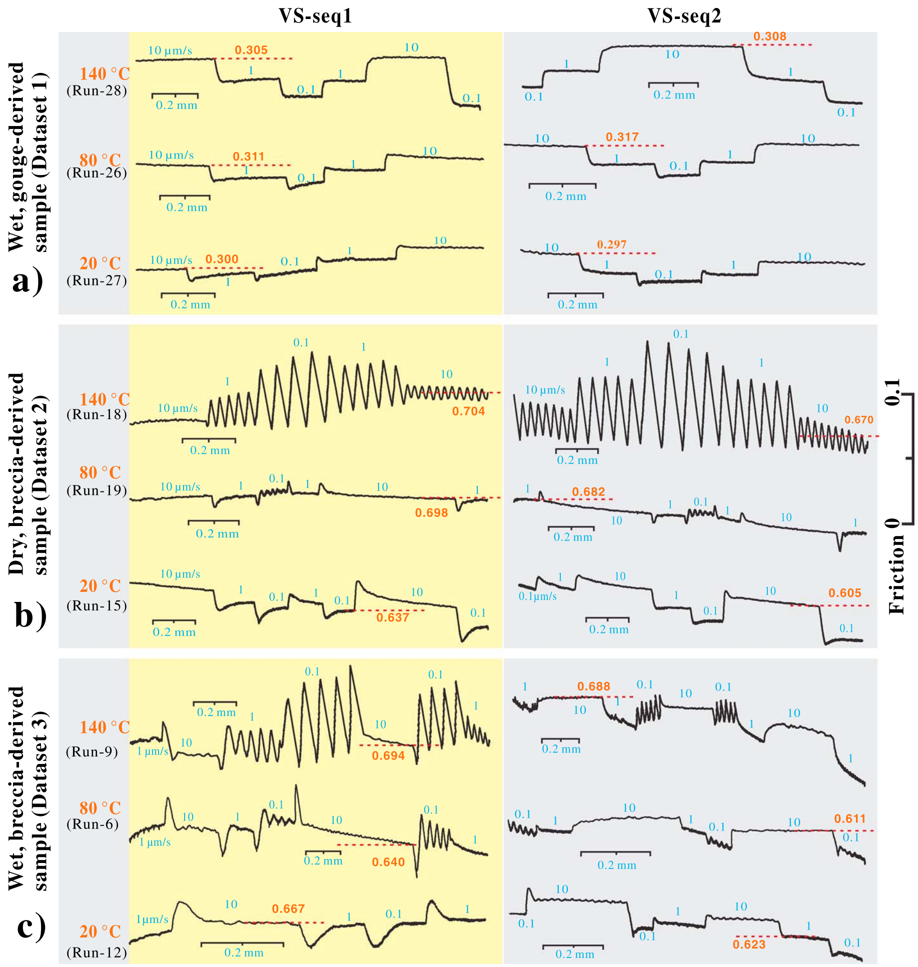

Figure 4. Velocity-stepping data obtained in the VS-seq1 and VS-seq2 stages of representative experiments performed on (a) wet gouge-derived samples, (b) dry breccia-derived sample, and (c) wet breccia-derived samples, at 20, 80, and 140°C. Individual sample numbers from Table 1 are as indicated. Friction coefficient scale bar (right) applies to all data sets. The absolute frictional strength level of each curve is marked by a dashed line. Velocities are indicated per step in μm/s.

(all wet) and from 0.64 to 0.72 for the breccia-derived samples (wet and dry). There is no consistent difference between dry and wet breccia-derived samples. The strengths of all samples falling in Data Sets 1–3 showed a tendency to increase with increasing temperature. Focusing now on slip stability, the wet, gouge-derived samples showed stable sliding behavior at all temperatures investigated (Figures 3 and 4). By contrast, the breccia-derived samples showed stable sliding at 20°C, transitioning to unstable slip (or stick slip) at elevated temperatures, under both dry and wet conditions (Figures 3 and 4). During SHS testing, wet gouge- and breccia-derived samples showed a progressive increase in (quasi) steady state friction upon reshearing, whereas dry breccia-derived samples showed more or less fixed steady state strength throughout each SHS sequence.

3.2. Velocity-Stepping Data

Representative velocity stepping or VS data obtained from the experiments performed on wet gouge-derived samples (Data Set 1), dry breccia-derived samples (Data Set 2), and wet breccia-derived samples (Data Set 3) are shown in Figure 4 (see also Table 1). For each data set, we compare typical VS-seq1 and VS-seq2 data for experiments performed at 20, 80, and 140°C. The $(a-b)$ values obtained, in all experiments reported under Data Sets 1–3, are plotted against temperature in Figure 5.

The wet gouge-derived samples showed stable, velocity-strengthening sliding behavior in all velocity steps and at all temperatures investigated (Figure 4a). Further quantification of the velocity dependence of friction in terms of $(a-b)$ showed that as temperature increases there is a systematic decrease in $(a-b)$, from an

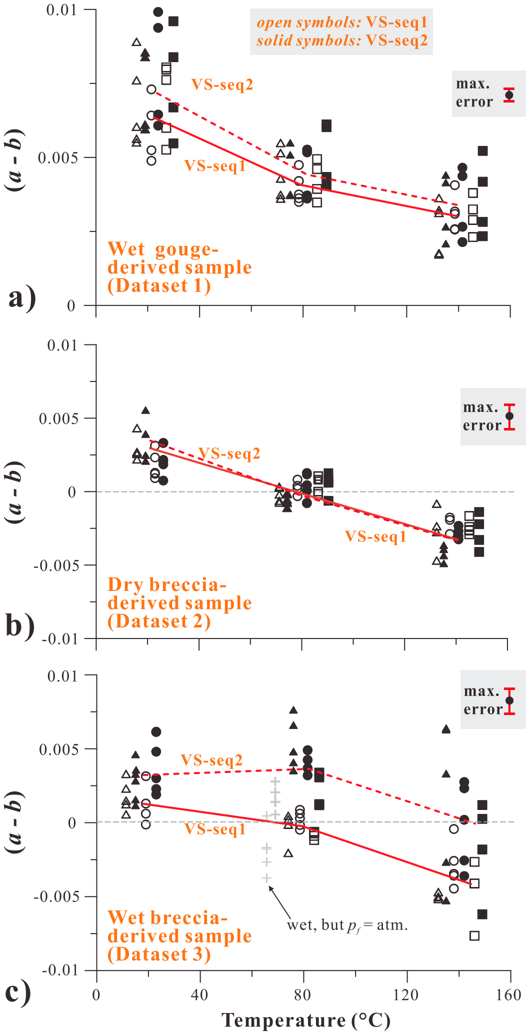

Figure 5. Temperature (*T*) dependence of the RSF rate dependence parameter $(a - b)$, determined from the velocity-stepping sequences performed before (VS-seq1) and after (VS-seq2) SHS testing, for the sample materials shown. All experiments were performed at an effective normal stress of 50 MPa. The open and solid symbols represent $(a - b)$ the values obtained in VS-seq1 and VS-seq2, respectively. The circles, squares, and triangles represent $(a - b)$ the values obtained in tests performed using reshearing velocities of, respectively, 0.1, 1, and 10 μm/s in the SHS stage (Table 1). The solid and dashed lines indicate the trends in average $(a - b)$ with temperature, for the VS-seq1 and VS-seq2 data, respectively. Note that the $(a - b)$ data obtained at each temperature (20, 80, and 140°C) are plotted at *T* values that are slightly displaced from the corresponding test temperature. This is done for plotting clarity.

average value of 0.0075 at 20°C to 0.003 at 140°C (Figure 5a). In addition, a slight increase in $(a - b)$ is evident for *V* steps (VS-seq2) performed after SHS testing relative to those performed before SHS testing (VS-seq1), as indicated in Figure 5a by the solid and dashed lines. This increase in $(a - b)$ occurred for all individual *V* steps (i.e., 0.1–1 μm/s, 1–10 μm/s, 1–0.1 μm/s, and 10–1 μm/s), although the magnitude of the increase was close to the error in $(a - b)$ (Figure 5a).

The dry breccia-derived samples (Figure 4b) showed (1) stable sliding plus velocity strengthening at 20°C, (2) velocity neutral or minor velocity-weakening behavior at ~80°C with oscillatory stick slips at the lowest slip rate of 0.1 μm/s, and (3) velocity weakening at 140°C with stick slips at all velocities. In line with this, $(a - b)$ decreases monotonically with increasing temperature over the full range of temperature investigated (Figure 5b), with a transition from velocity strengthening to velocity weakening occurring at ~80°C. These samples showed no significant difference in the $(a - b)$ values determined before versus after SHS testing. The only difference we found was that the stick slips seen in the VS-seq2 stage of the experiments performed at 140°C showed larger amplitude than in the VS-seq1 stage of the same experiments (Figure 4b), implying reduced stability in the VS-seq2.

For the wet breccia-derived samples, the first VS sequence (VS-seq1) showed similar behavior to that exhibited by the dry samples in VS-seq1 (or VS-seq2) at the same conditions (Figure 4c). Though slightly more scattered, the $(a - b)$ values determined for the wet samples in VS-seq1 also showed a negative temperature dependence and a transition from velocity-strengthening to velocity-weakening slip at ~80°C (Figure 5c). However, the second VS sequence (VS-seq2) showed higher, mostly positive $(a - b)$ values, decreasing to more or less zero on average at 140°C, implying a tendency for more stable slip behavior at all temperatures investigated (Figure 4c). This stabilization effect was also reflected by a decrease in stick-slip amplitude in the VS-seq2 stage of the experiments relative to the VS-seq1 stage (Figure 4c). Note that in the post-SHS sequences (VS-seq2), the higher $(a - b)$ values and a slightly wider variability in $(a - b)$ resulted in velocity weakening and marked stick slips occurring only at 140°C (Figures 4c and 5c). The average increase in $(a - b)$ values in VS-seq2 compared with VS-seq1, as indicated by the gap between the solid and dashed red lines in Figure 5c, was ~0.0042. This value is larger than the maximum error of ±0.0017 in $(a - b)$ displayed in Figure 5c, implying a true increase in $(a - b)$ after SHS testing. This increase in $(a - b)$ was evident in all *V* steps.

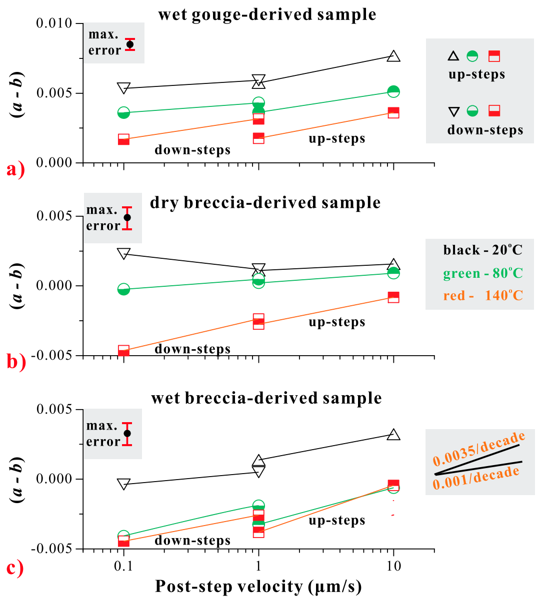

Figure 6. Velocity dependence of $(a-b)$, determined from the velocity-stepping data for (a) wet gouge-derived and (b) dry and (c) wet breccia-derived samples sheared at different temperatures. For each sample and each temperature (20, 80, and 140°C), only $(a-b)$ data from the VS-seq1 data are plotted. The legend and slope indicators (right) apply to all data sets.

Lastly, we examine the effect of sliding velocity on $(a-b)$. All our data sets, i.e., the wet gouge-derived, dry breccia-derived, and wet breccia-derived samples, showed similar effects of velocity, in both the VS-seq1 and VS-seq2 stages of the experiments. For plotting clarity, we illustrate the observed behavior for one experiment per sample type (i.e., for Data Sets 1–3), focusing on the VS-seq1 data only—see Figure 6. The results demonstrate that the $(a-b)$ values obtained for V steps of 1–10 µm/s are always larger than that for V steps of 0.1–1 µm/s with the same sense of stepping, i.e., upward or downward. This trend holds for all the three data sets (Figures 6a–6c), suggesting that $(a-b)$ tends to increase with increasing load point velocity, with slopes ranging from 0.001 to 0.0035 per decade change in velocity.

3.3. Slide-Hold-Slide Data

3.3.1. Slide-Hold-Slide Curves

The slide-hold-slide data obtained for the wet gouge-derived, dry breccia-derived, and wet breccia-derived samples (Data Sets 1–3, Table 1) are presented in Figures 7a–7c, respectively. Broadly speaking, using the terminology defined in section 2.4 (Figure 2b) [*Chen et al.*, 2015], and removing background slip weakening and strengthening trends, we observed three kinds of frictional healing behavior (Figure 7 and Table 1):

Type 1a healing behavior with $\Delta\mu_{pk} = \Delta\mu_w > 0$ and $\Delta\mu_{pk} = \beta \log\,(1 + t_h/t_c)$, where t_c is a cutoff time on the order of 1 s. This is Dieterich-type healing behavior, where β refers to the healing rate. Note that Type 1b healing, for which $\Delta\mu_{pk} = \Delta\mu_w > 0$ but the logarithmic relation is not obeyed, was not observed in the present study.

Type 2 healing behavior with $\Delta\mu_{pk} > \Delta\mu_w > 0$. This is characterized by an increase in (quasi) steady state friction coefficient after reshearing ($\Delta\mu_r > 0$).

Type 3 healing behavior with $\Delta\mu_{pk} = \Delta\mu_r < 0$ and $\Delta\mu_w = 0$. This is characterized by the absence of a peak, therefore by zero postpeak weakening effect ($\Delta\mu_w = 0$).

We now make use of this terminology and the associated parameters to describe the trends in healing behavior shown by experiments in Data Sets 1–3. First, we note that all experiments show an increase in the magnitude of stress relaxation ($\Delta\mu_c$) with increasing V_{SHS} and increasing hold time t_h and a decrease with increasing temperature (Figure 7). The wet breccia-derived samples relaxed more than the dry breccia-derived samples but less than the wet gouge-derived samples at otherwise similar conditions. With continued reference to Figure 7, the behavior seen upon subsequent resharing can be described as follows for each data set.

1. Wet gouge-derived samples. At 20°C and for V_{SHS} of 0.1 and 10 µm/s, these samples display Type 3 healing behavior, while the sample tested at V_{SHS} of 1 µm/s (Run 27, Table 1) shows Type 1a healing behavior. No clear trends are visible in these few data at 20°C (Figure 7a). By contrast, the samples tested at elevated temperatures (80 and 140°C) show Type 2 healing behavior ($\Delta\mu_{pk} > \Delta\mu_w$, Figure 7a), whereby the peak healing ($\Delta\mu_{pk}$) and postpeak weakening ($\Delta\mu_w$) parameters increase with increasing T, t_h, and V_{SHS}. The persistent restrengthening ($\Delta\mu_r$) exhibited by these samples also increases with T and V_{SHS} and possibly irregularly with hold time.
2. Dry breccia-derived samples. These show Dieterich-type (Type 1a) healing behavior, with $\Delta\mu_{pk} = \Delta\mu_w$ tending to increase with increasing T, t_h, and V_{SHS} (Figure 7b). As seen in the VS data, stick slips also occurred during the sliding portion of the SHS sequences performed on these samples at 140°C.

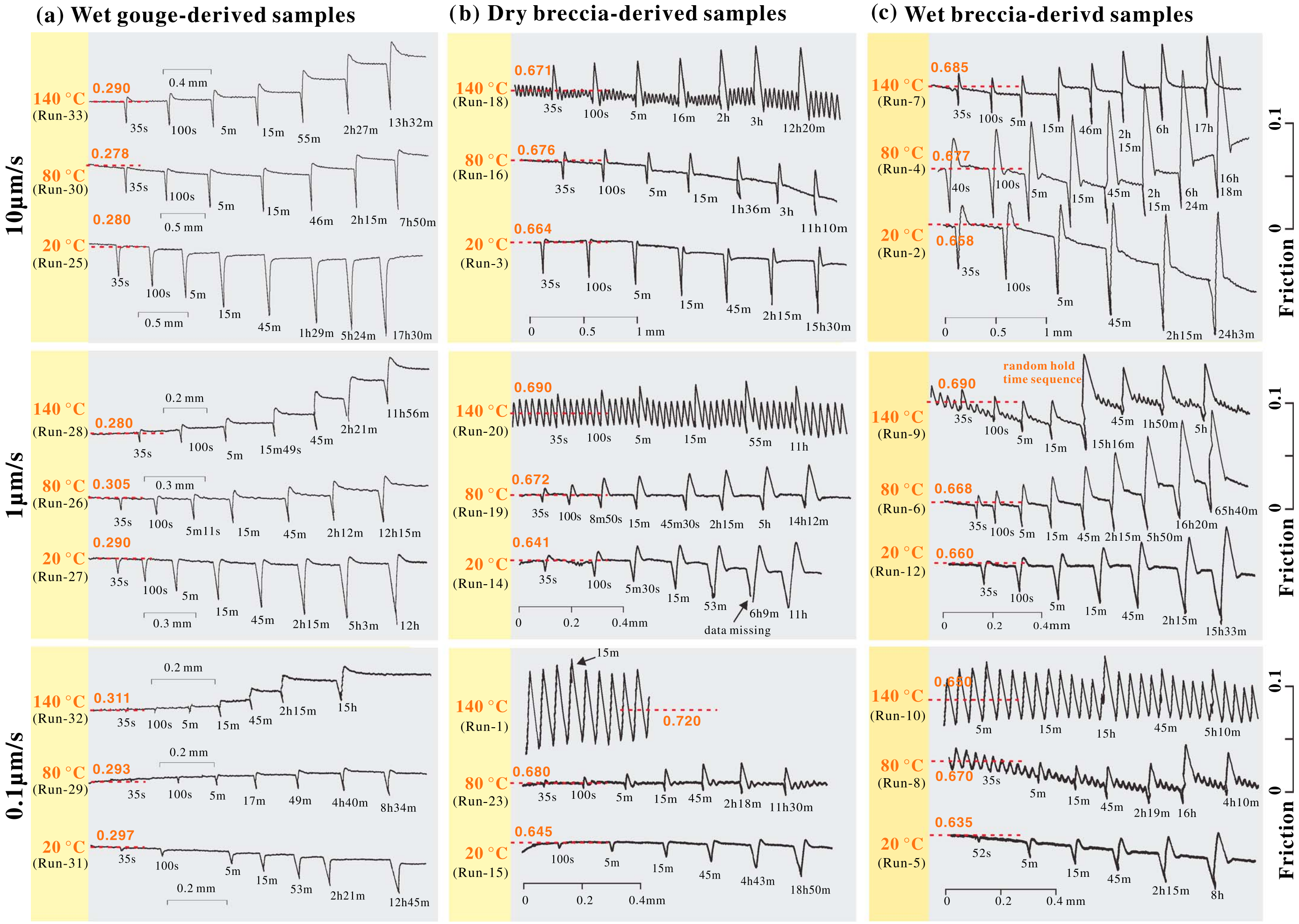

Figure 7. SHS results for (a) the wet gouge-derived samples, (b) dry breccia-derived samples, and (c) wet breccia-derived samples. For each set of experiments, a range of temperatures (20, 80, and 140°C) and load point velocities (0.1, 1, and 10 μm/s) was investigated.

3. Wet breccia-derived samples. At 20°C, the wet breccia-derived samples display Dieterich-type (Type 1a) healing behavior. However, at elevated temperatures (80 and 140°C), these samples exhibit Type 2 healing behavior, with $\Delta\mu_{pk}$ and $\Delta\mu_w$ increasing with increasing t_h and (crudely) with increasing shearing velocity V_{SHS} (Figure 7c). The corresponding $\Delta\mu_r$ values increase with t_h over the first few SHS events ($t_h < 60{,}000$ s) but then level off to finally cease changing over long hold periods (Figures 3 and 7c). Note that the magnitude of healing ($\Delta\mu_{pk}$ and $\Delta\mu_w$) observed in the wet breccia-derived samples is always larger than in the dry equivalents ($\Delta\mu_{pk} = \Delta\mu_w$) at otherwise similar conditions and that positive $\Delta\mu_r$ is only seen in the wet samples. Stick-slip occurred during the sliding portion of the SHS sequences performed on these samples at 140°C for V_{SHS} of 1 and 0.1 μm/s and at 80°C for V_{SHS} of 0.1 μm/s.

3.3.2. Healing Magnitude Parameters Versus log(t_h)

The healing magnitude parameters $\Delta\mu_c$, $\Delta\mu_{pk}$, $\Delta\mu_w$, and $\Delta\mu_r$ obtained from SHS testing are plotted against the logarithm of hold time in Figure 8. Specifically, the results for the wet gouge-derived, dry breccia-derived, and wet breccia-derived samples are shown in Figures 8a–8c, respectively. Comparison of these results shows that, in all cases, the magnitude of stress relaxation ($\Delta\mu_c$) increases more or less linearly with log(t_h) (Figures 8a–8c), with the effect being most marked in the wet, gouge-derived samples. The following observations emerge with respect to $\Delta\mu_{pk}$, $\Delta\mu_w$, and $\Delta\mu_r$.

1. Wet gouge-derived samples. These samples show a direct, near-linear relation between $\Delta\mu_w$ and log(t_h). By contrast, the transient peak healing and postpeak weakening parameters ($\Delta\mu_{pk}$ and $\Delta\mu_r$) generally show an increase with log(t_h) at relatively short hold periods ($<10^4$ s), followed by a decrease at longer

(a) Wet gouge-derived samples

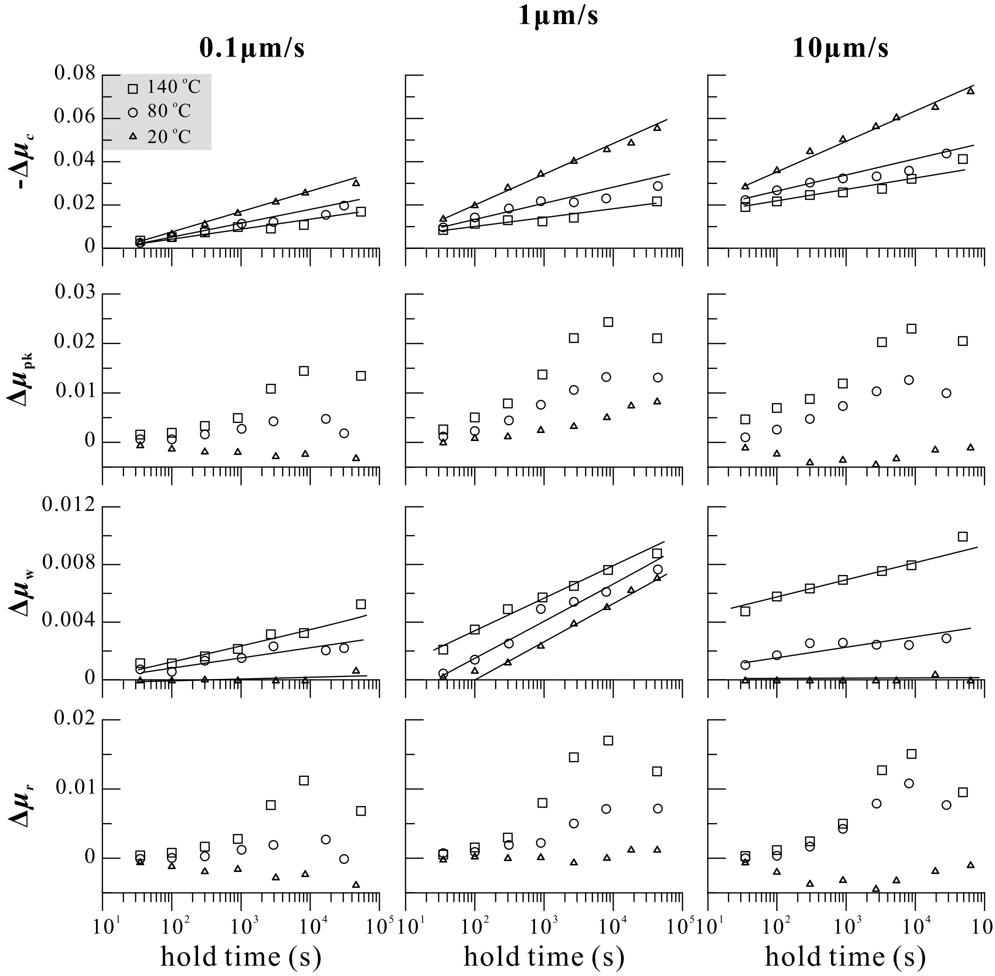

(b) Dry breccia-derived samples

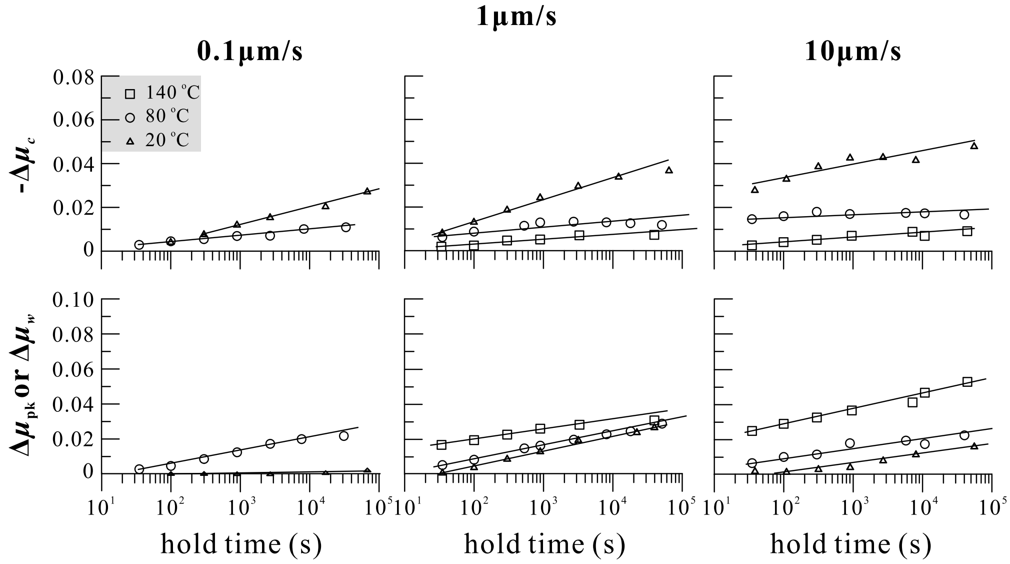

Figure 8. Frictional healing and relaxation parameters plotted as functions of the logarithm of hold time, for (a) the wet gouge-derived, (b) dry breccia-derived, and (c) wet breccia-derived samples. For each material, we present the data obtained across the full range of temperatures and load point velocities investigated. Note that $\Delta\mu_c$ corresponds to shear stress relaxation, μ_{pk} to the transient peak healing, μ_w to the postpeak frictional weakening, and μ_r to persistent strengthening.

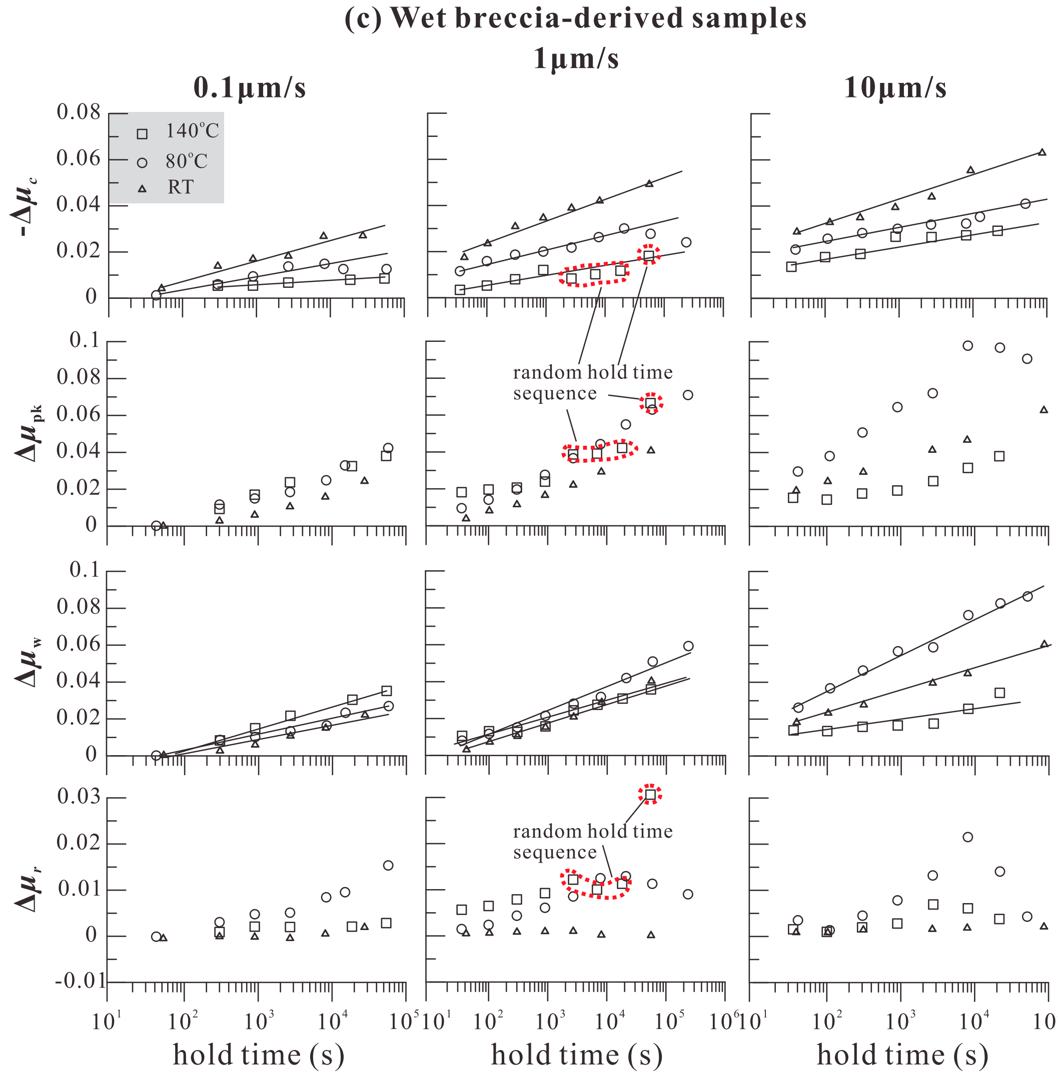

Figure 8. (continued)

hold periods (Figure 8a). Where Type 3 healing behavior was encountered, i.e., in those samples deformed at 20°C and showing negative $\Delta\mu_{pk}$, no clear trend in $\Delta\mu_r$ is visible (Figure 8a).

2. Dry breccia-derived samples. In these samples, the transient peak healing and postpeak weakening parameters ($\Delta\mu_{pk} = \Delta\mu_w$) increase roughly linearly with the logarithm of hold time (Figure 8b), confirming Type 1a or Dieterich-type healing.
3. Wet breccia-derived samples. Some samples show $\Delta\mu_{pk}$ being more or less linearly proportional to log(t_h), while others show a poor correlation (Figure 8c). The $\Delta\mu_r$ data also show parallel trends. However, the postpeak weakening ($\Delta\mu_w$) displayed by these samples is mostly very well described by a linear relation versus log(t_h) (Figure 8c).

In summary, our results on healing parameters versus log(t_h) demonstrate that the peak healing or restrengthening effect ($\Delta\mu_{pk}$) observed in wet experiments on gouge- and breccia-derived samples essentially comprises two components. These consist of a component $\Delta\mu_w$, which is linearly proportional to log(t_h) in a manner resembling Dieterich-type healing, plus a persistent increase in (quasi) steady state friction coefficient $\Delta\mu_r$. The latter shows a maximum value at hold times on the order of 10^4 s (Figures 8a and 8c), except in the run we performed using a random hold time sequence (Run 9, Table 1 and Figures 7c and 8c for the SHS data). Typical results explicitly illustrating this partitioning of $\Delta\mu_{pk}$ into $\Delta\mu_w$ and $\Delta\mu_r$, in the wet gouge- and breccia-derived samples, are replotted from Figure 8 in Figures 9a and 9b, respectively.

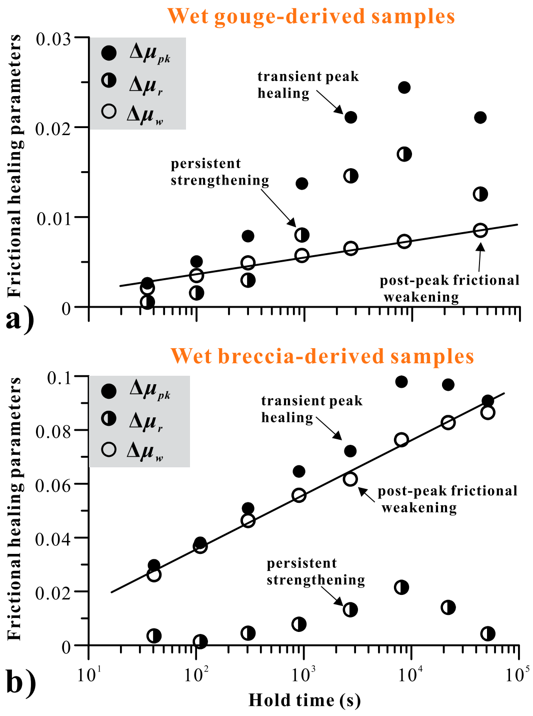

Figure 9. Typical frictional healing results for (a) wet gouge-derived and (b) wet breccia-derived samples, illustrating partitioning of healing seen in SHS stages. Data in Figure 9a are from Run 22 performed at 140°C using V_{SHS} of 1 μm/s. Data in Figure 9b are from Run 4 performed at 80°C using V_{SHS} of 10 μm/s. In both cases, the peak healing ($\Delta\mu_{pk}$) observed essentially consists of two components, i.e., a persistent strengthening in dynamic friction ($\Delta\mu_r$ effect) plus a Dieterich component ($\Delta\mu_w$ effect).

By contrast, the results obtained in our dry experiments on breccia-derived samples are characterized by $\Delta\mu_{pk} = \Delta\mu_w$ and $\Delta\mu_r = 0$, which corresponds to classical Dieterich-type healing.

3.3.3. Relaxation and Healing Rates

Shear stress relaxation rates during hold periods were obtained for all samples (Data Sets 1–3), using the parameter defined as $\rho = d(-\Delta\mu_c)/d(\log_{10}(t_h))$, analogue to the definition of frictional healing rate. The values obtained lie in the ranges shown in Figure 10. For all SHS tests performed, ρ displayed a negative dependence on temperature and a positive dependence on V_{SHS} (Figure 10). For given values of V_{SHS} and T, wet breccia-derived samples always relaxed faster than dry breccia-derived samples but more slowly than the wet gouge-derived samples (Figure 10).

Frictional healing rates occurring in the SHS stage of our experiments were quantified using the parameter $\beta_x = d(\Delta\mu_x)/d(\log_{10}(t_h))$, where the subscript "$x$" refers to either "$pk$" or "$w$." Note that some of the $\Delta\mu_{pk}$ data show a complex dependence on $\log_{10}(t_h)$ (see Figure 8). For consistency, β_{pk} fits are nonetheless added for comparison (gray symbols and gray dashed lines, Figure 10). For all SHS runs performed in this study, healing rate fits to our $\Delta\mu_w$ versus $\log_{10}(t_h)$ data yielded β_w values ranging from 0 to 0.0023/decade for the wet gouge-derived samples, from 0.0011 to 0.0086/decade for the dry breccia-derived samples ($\beta_w = \beta_{pk}$), and from 0.0097 to 0.0196/decade for the wet breccia-derived samples (Figure 10). The rate of transient peak healing β_{pk} was slightly (~1.1 times) higher than β_w for the wet breccia-derived samples at all temperatures investigated, while for the wet gouge-derived samples, β_{pk} values were much higher (~5 times at 80°C and ~4 times at 140°C) than β_w. For the dry breccia-derived samples, which showed classical Dieterich-type healing, β_w and β_{pk} values were of course equal, as indicated above. In general, β_{pk} and β_w increased with temperature, except in wet breccia-derived material between 80°C and 140°C. Even though the magnitude of healing ($\Delta\mu_{pk}$ and $\Delta\mu_w$) was always larger for higher V_{SHS}, the rate parameters β_{pk} and β_w do not show a consistent dependence on V_{SHS} for any sample type (Data Sets 1–3).

We now consider the rate of development of $\Delta\mu_r$ during hold periods, for the samples that showed positive values of this parameter, i.e., the wet gouge- and wet breccia-derived samples at 80 and 140°C (Figures 8a and 8c). Plotting $\Delta\mu_r$ against t_h or $\log(t_h)$ for these samples does not yield any systematic relationships such as those seen for $\Delta\mu_{pk}$ or $\Delta\mu_w$ (e.g., Figures 8 and 9). Rather, in the SHS sequences, the steady state friction in some of these samples seems to become "saturated," causing $\Delta\mu_r$ to gradually approach zero in long hold periods—see Figures 7a, 7c, 8a, and 8c. It is apparent from these figures that there is a positive dependence of $\Delta\mu_r$ on V_{SHS}.

3.4. Results of Control Experiments on Breccia-Derived Samples

The control experiments performed on breccia-derived samples using alternative pore fluids to sample-saturated water (Data Set 4, Table 1) yielded the following results. First, the use of phosphate solution yielded lower $(a-b)$ and healing parameter values ($\Delta\mu_r$, $\Delta\mu_{pk}$, and $\Delta\mu_w$) compared with "normal" wet experiments in breccia-derived samples (Figure 11a). An increase in $(a-b)$ in VS-seq2 relative to VS-seq1 also

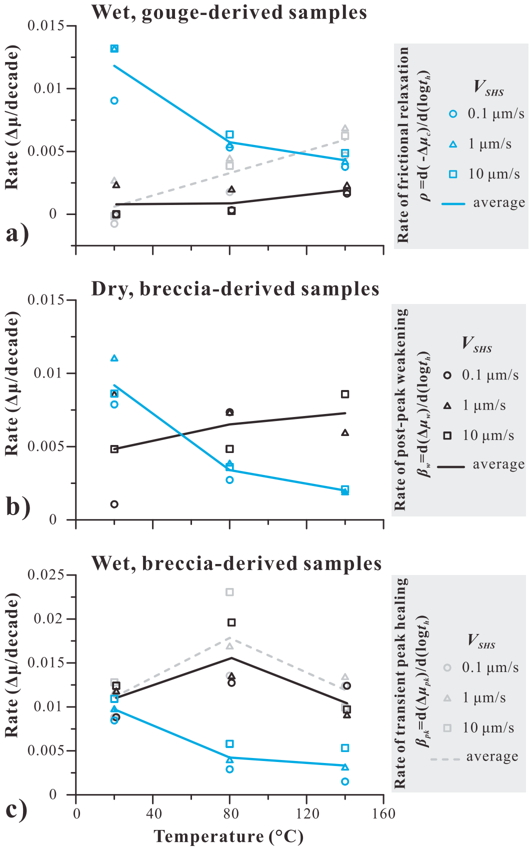

Figure 10. Frictional healing rates (β) and relaxation rates (ρ) plotted as a function of temperature, for (a) wet gouge-derived, (b) dry breccia-derived, and (c) wet breccia-derived samples. The blue, gray, and black symbols indicate the rates of frictional relaxation ρ ($-\Delta\mu_c$/decade), frictional healing β_{pk} ($\Delta\mu_{pk}$/decade), and β_w ($\Delta\mu_w$/decade), respectively. The circular, triangular, and square symbols represent the imposed SHS velocities (V_{SHS}) of 0.1, 1, and 10 μm/s, respectively. The blue, dashed gray, and black lines represent the trends in the average values of the corresponding rate parameter.

occurred in these runs. However, in view of the uncertainties in $(a-b)$ (e.g., Figure 5), it is unclear how significant the apparent changes in $(a-b)$ are compared with normal wet experiments (Data Set 3). Second, the experiments conducted using silicone oil as pore fluid showed behavior similar to dry samples tested at similar conditions (i.e., Type 1a healing during SHS testing and no change in $(a-b)$ between two VS-seqs) (Figure 11b), except for a few stress fluctuations occurring before reaching the macroscopic yield point. Finally, in the single experiment performed on a water-saturated, breccia-derived sample (Run 13) at atmospheric pore pressure, the $(a-b)$ values obtained are systematically lower than normal wet experiments performed using pressurized pore fluid (Figure 11c). Nonetheless, an increase in $(a-b)$ in VS-seq2 relative to VS-seq1 is still present (Figures 5c and 11c).

The control experiments performed on wet breccia-derived samples but using nonstandard SHS procedures (Runs 2, 4, and 9 in Data Set 3, annotated with "b"–"e" in Table 1) also showed interesting effects. Those employing an increasing hold time sequence followed by a decreasing sequence (Run 2 and Run 4) exhibited Type 2 healing behavior in both sequences (Figure 11d). However, for the same duration of holds, $\Delta\mu_r$ obtained in the decreasing sequence was much smaller compared with that in the increasing sequence. In the run performed using randomly varied hold times (Run 9), the early long hold generated abnormally large $\Delta\mu_r$ and thus $\Delta\mu_{pk}$ compared with the normal tests (Figure 7c), although the $\Delta\mu_w$ data still showed a linear relation with $\log(t_h)$ (Figure 8c). The test employing velocity stepping only (Run 17, Table 1) indicated that the friction rate dependence parameter $(a-b)$ does not change with displacement alone (Figure 11e). Lastly, the experiment employing one hold period only (Run 11, Table 1) also displayed positive $\Delta\mu_r$, as well as an increase in $(a-b)$ immediately after the hold period (Figure 11f).

3.5. Compaction Data

Thickness change data, referred to here as compaction data, were obtained only for wet breccia-derived samples—see Figure 12a. These samples showed marked compaction in the first 200–300 s or 0–1.5 mm of shear deformation, i.e., during initial hardening in the approach to macroscopic yield (cf. Figure 3). Beyond this initial loading phase, the compaction curves exhibit a clear decrease in compaction rate with time (indicated by the decreasing slope in Figure 12a). For comparative purposes, friction coefficient and compaction versus displacement data are presented in the inset in Figure 12a, for a typical SHS testing sequence (Run 6) performed on wet breccia-derived samples at 80°C. These data demonstrate an increase in gouge compaction with hold time but no significant changes upon resliding or during sliding periods. Using the compaction (ΔL) and hold time (t_h) data obtained from the SHS phase of all experiments on wet, breccia-derived samples, we calculated the average compaction strain rate for each hold period using the equation $\dot{\varepsilon} = \Delta L/(L_0 t_h)$, where L_0 is the initial sample thicknesses assumed to be 0.8 mm (see Text S2). As

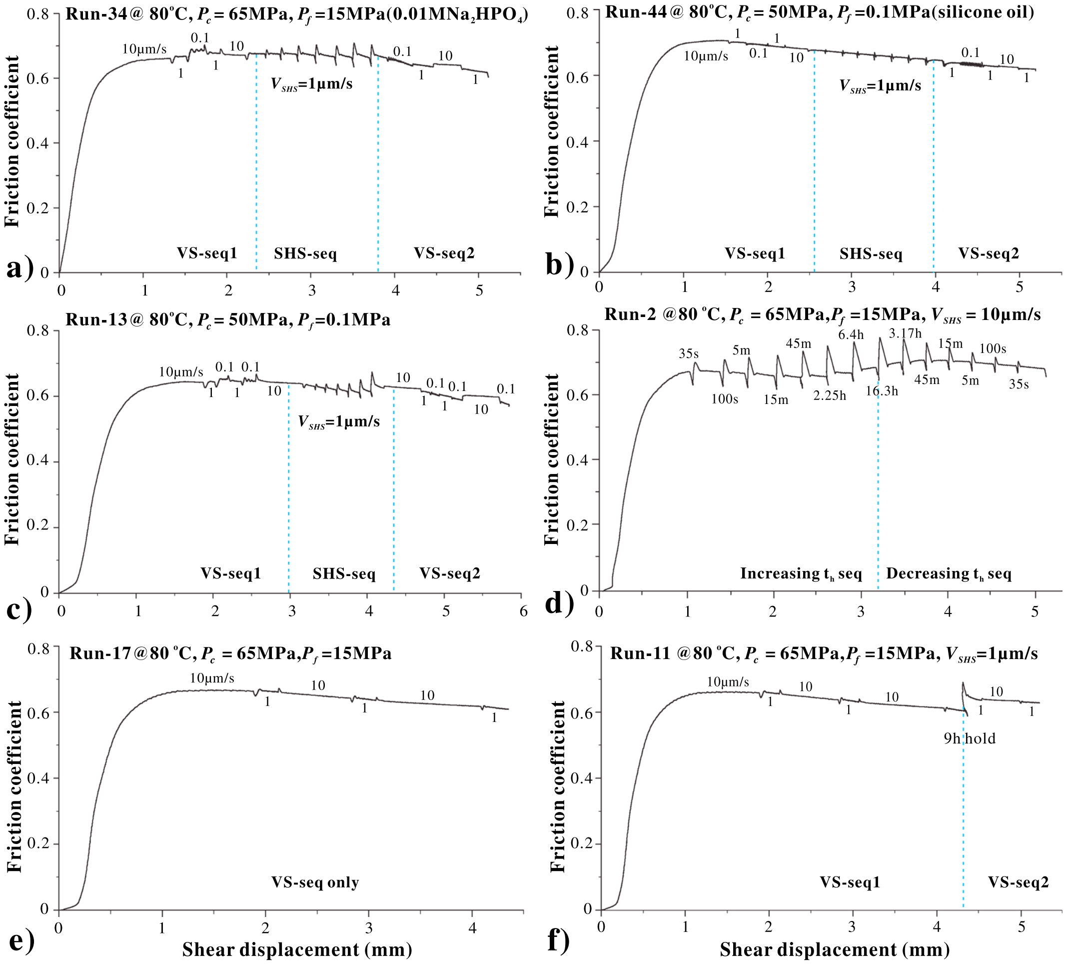

Figure 11. Representative results obtained from the various control experiments performed on breccia-derived samples using different pore fluids (Data Set 4, Table 1) and nonstandard VS and SHS testing sequences (see Data Sets 3b–3e, Table 1). All the experiments were performed at 50 MPa effective pressure and 80°C. (a) The 0.01 *M* NaH_2PO_4 solution as pore fluid (Run 34); (b) silicone oil as pore fluid (Run 44); (c) sample-saturated demineralized water as pore fluid but drained to the atmosphere (Run 13); (d) a pure-SHS test, in which both forward and backward hold times were used (Run 2); (e) a run with velocity-stepping sequence only (Run 17); and (f) a test in which the SHS sequence contained one hold period only (Run 11).

shown in Figures 12b and 12c, the resulting compaction strain rates, calculated for all wet breccia-derived samples, show a decreasing trend with increasing temperature and an increasing trend with increasing reshearing velocity (V_{SHS}).

The total compaction of the gouge layer in each experiment (Data Sets 1–3) was also obtained from the thickness change of the sample assembly before versus after the experiment. Since all samples were prepared with approximately the same initial thickness (1 ± 0.05 mm), the final thickness yields a direct indication of compaction magnitude, including any minor extrusion of material from the assembly during shear (Table 1). For the wet gouge-derived samples, the dry and wet breccia-derived samples, the mean compaction values calculated in this way, regardless of temperature, are 0.36, 0.31, and 0.15, respectively.

It should be noted that the resolution of our volumetric measurements for monitoring sample thickness change was ~3 μm, which is much poorer than achieved for displacement measurement [cf. *Yasuhara et al.*, 2005]. This means that only dynamic thickness changes bigger than this value, occurring in response to a long hold period, for example, can be reliably detected. For most of our SHS tests that have short hold periods, i.e., $t_h < 10{,}000$ s, dilatation upon reshear was simply below the detection level (for details, see *Chen et al.* [2015]).

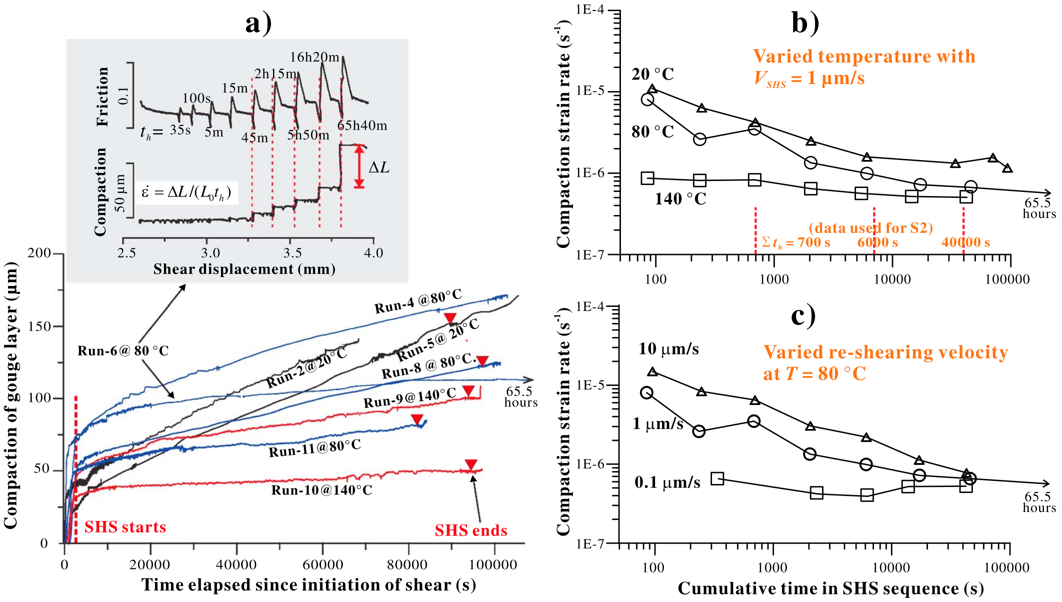

Figure 12. Gouge compaction and compaction strain rate data for the wet breccia-derived samples. (a) Gouge compaction data for entire experiments (since the touch point). (b and c) Compaction strain rate versus cumulative hold time during SHS testing phase. In Figure 12a, the black, blue, and red lines indicate the results from experiments performed at 20, 80, and 140°C, respectively. The curves have been smoothed by averaging the original data obtained for every 100 data points (10 s). The inset graph in Figure 12a illustrates the gouge compaction/dilatation as a function of displacement during the SHS sequence, from which compaction strain rate was determined using the equation shown. In Figure 12b, calculated compaction strain rates are plotted as a function of the logarithm of time, for experiments performed at different temperatures (20, 80, and 140°C), while Figure 12c shows the similar data plotted for different resliding velocities (0.1, 1, and 10 µm/s).

4. Discussion

4.1. General Features of the Present Experiments

The present results show frictional strengths of 0.64–0.72 for the dry and wet breccia-derived samples studied versus of 0.30–0.34 for wet gouge-derived samples (Table 1). These values are in agreement with previous results on carbonates and on clay-rich gouges obtained at room temperature [e.g., *Tembe et al.*, 2010; *Scuderi et al.*, 2013; *Verberne et al.*, 2013b]. Moreover, the frictional strengths for all samples tested showed a tendency to increase with increasing temperature within the range investigated (Figure 3 and Table 1). Positive temperature-dependent frictional strengths have also been widely observed on other material [*Verberne et al.*, 2013b; *den Hartog et al.*, 2013].

We observed the same broad dependence of $(a - b)$ on temperature for breccia-derived samples as reported for calcite-rich gouges by *Verberne et al.* [2013b] and by *Chen et al.* [2015], leading to a transition from velocity strengthening to velocity weakening with increasing temperature (Figures 4 and 5). By contrast, the gouge-derived samples exhibited stable, velocity-strengthening slip at all the temperatures investigated, although a negative temperature dependence of $(a - b)$ was present (Figure 5). We also observed a positive dependence of $(a - b)$ on slip rate for all samples tested, with $(a - b)$ increasing at a rate of 0.001–0.0035 per decade change in velocity (Figure 6). All these aspects of behavior are similar to previous findings for both carbonate- and phyllosilicate-rich gouges [*Weeks and Tullis*, 1985; *Ikari et al.*, 2009; *Verberne et al.*, 2013a].

In addition, we have found a variety of more unusual history effects made visible by the sequential application of VS, SHS, and VS stages in the present experiments. Dry experiments on breccia-derived samples show classical Dieterich-type healing, with no effects of SHS testing on friction rate dependence, $(a - b)$. By contrast, the wet tests on breccia-derived samples show (1) an increase in steady state friction upon resliding after a hold period and (2) a pronounced increase in $(a - b)$, after the SHS stage. These effects are visible in wet experiments performed at elevated temperatures but are absent from experiments on either dry samples or wet samples tested at 20°C (Figures 5, 7, and 8). These findings confirm our previous, preliminary data on the same sample breccia-derived gouge [*Chen et al.*, 2015]. Surprisingly, though, our results show that these unusual effects are also present in our experiments performed on gouge-derived samples at hydrothermal conditions, despite the fact that these two materials have quite different mineral compositions.

In the following discussion, we will quantitatively analyze how the magnitudes and rates of the direct, peak frictional healing effect that we observed (i.e., $\Delta\mu_{pk}$) depend on the various factors investigated in this study, i.e., temperature, reshearing velocity, mineral composition, and the presence of pore fluid, and to what extent the different components (i.e., $\Delta\mu_w$ and $\Delta\mu_r$) contribute to the peak healing ($\Delta\mu_{pk}$). We go to discuss the possible mechanism(s) responsible for the observed behavior, and we consider the implications of our results for the LFZ and for faults in tectonically active carbonate terrains in general. Finally, we compare our results with limited similar findings for other gouge materials [e.g., *Yasuhara et al.*, 2005] in an attempt to draw some broader conclusions.

4.2. Factors Influencing Frictional Healing

4.2.1. Effect of Temperature

In the present experiments on wet gouge-derived samples, and on wet and dry breccia-derived samples, we observed a systematic increase in the magnitude of frictional healing (i.e., posthold restrengthening $\Delta\mu_{pk}$), and in healing rate (β_{pk}) with increasing temperature in the range of 20 to 140°C, expect in the case of wet breccia-derived material at 80 and 140°C where the reverse trends were recorded (Figures 7 and 8). In particular, wet gouge-derived samples (Figure 10a) show an increase in average healing rate (β_{pk}) by ~10 times, from 0.0006/decade measured at 20°C to 0.0059/decade at 140°C.

Thermally enhanced frictional healing, similar to that seen in all but wet breccia-derived samples at higher temperatures, has been observed in experiments on wet quartz gouge up to 200°C [*Nakatani and Scholz*, 2004], on dry feldspar gouge up to 600°C [*Nakatani*, 2001], and on dry bare granite surfaces up to 550°C [*Mitchell et al.*, 2012]. Viewed in the framework of RSF laws, frictional healing rates (β_{pk}) are expected to scale with the evolution parameter *b* for long hold times [e.g., *Marone*, 1998a; *Baumberger et al.*, 1999]. At the same time, theoretical analyses that assume that friction is controlled by a thermally activated mechanism indicate that *b* should be proportional to absolute temperature [*Bréchet and Estrin*, 1994; *Nakatani and Scholz*, 2004]. Thus, β_{pk} should increase in direct proportion to absolute temperature, that is $\beta_{pk} \propto T$. Assuming a temperature change from 20°C (293 K) near the surface to 250°C (523 K) at the base of the seismogenic zone for a carbonate fault (i.e., at 10 km depth), the implication is that healing rates across this range should roughly double. This is reasonably consistent with the variation in healing rates ($\beta_{pk} = \beta_w$) observed in our dry experiments (Figure 10b). Similar sensitivities of healing rate (β_{pk}) to absolute temperature have also been reported for dry feldspar and wet quartz gouges [*Nakatani*, 2001; *Nakatani and Scholz*, 2004]. However, the β_{pk} values observed in our wet experiments do not agree with this model prediction. In our runs on wet gouge-derived samples (Figure 10a), the increase in β_{pk} with temperature that we observed is far in excess of this model prediction, even though the temperature range investigated spanned only 20 to 140°C. In addition, the β_{pk} data obtained for wet breccia-derived samples displayed an increase and then a decrease with increasing temperature (Figure 10c). All this suggests that the direct effect of absolute temperature on healing embodied in previous models [*Bréchet and Estrin*, 1994; *Nakatani*, 2001; *Mitchell et al.*, 2012], though consistent with our results for dry breccia-derived samples, cannot fully account for the more rapid healing observed in our wet experiments on both gouges studied. This means that other effects must play a role.

4.2.2. Effect of Resliding Velocity

Independently of temperature, our results for all the samples tested show an increase in the magnitudes of frictional healing, i.e., in $\Delta\mu_{pk}$ and $\Delta\mu_w$, with increasing sliding velocity (V_{SHS}), as implemented in the SHS sequences (see Figure 8), except for a few wet tests run at between 1 and 10 μm/s (Runs 3, 16, and 25). However, the healing rates (β_{pk} and β_w) obtained do not show a consistent trend with V_{SHS} (Figure 10). Previous experiments on dry quartz gouge and dry salt/salt interface, performed at room temperature, also report a strong increase in frictional healing ($\Delta\mu_{pk}$) with increasing SHS velocity and a weak dependence of healing rate on reshearing velocity [*Marone*, 1998b; *Renard et al.*, 2012]. These findings are thus broadly consistent with our results. The $\Delta\mu_r$ data obtained in our experiments at hydrothermal conditions, for both the gouge- and breccia-derived samples, show a tendency to increase with increasing reshearing velocity (Figures 8a and 8c).

Marone and Saffer [2015] recently carried out numerical modeling to investigate the effect of loading rate on frictional healing ($\Delta\mu_{pk}$ in our definition), based on the standard RSF equations. Their results show that the role of reshearing velocity (V_{SHS}) in determining healing is the same as that of V steps in determining the direct response to a velocity jump, with the magnitude of healing being proportional to the logarithm of V_{SHS} implemented. This may explain the healing observed in our dry experiments or the Dieterich-type component of healing ($\Delta\mu_w$) found in hydrothermal experiments. However, it cannot explain the total healing effect ($\Delta\mu_{pk}$) or the residual healing effect ($\Delta\mu_r$) observed in our runs showing Type 2 healing behavior. The origin of persistent strengthening ($\Delta\mu_r$) therefore remains unclear at this point. This healing effect and the role of reshearing rate are not readily embodied in the standard RSF laws. Alternative models are therefore needed.

4.2.3. Presence of Water (Wet Versus Dry Breccia-Derived Samples)

Comparison of our results for dry and wet breccia-derived samples clearly indicates that addition of water causes enhanced frictional healing (Figures 8b and 8c). Since the peak healing ($\Delta\mu_{pk}$) observed in the wet samples at elevated temperatures is essentially composed into two components (i.e., $\Delta\mu_{pk} = \Delta\mu_w + \Delta\mu_r$), we thus interpret the difference between the peak healing ($\Delta\mu_{pk}$) observed in wet samples and dry samples at otherwise similar conditions (i.e., t_h, V_{SHS}, and elevated T) to reflect a combination of fluid-assisted effects influencing the Dieterich component ($\Delta\mu_w$) and producing the extra healing effect ($\Delta\mu_r$). As shown in Figure 10b, the healing rates (β_w) reported for the dry breccia-derived sample fall in the range of 0.0018–0.0085/decades. However, the Dieterich component (β_w) reported here for the wet breccia-derived sample ranges from 0.0088 to 0.0196/decade. The healing rates are even higher (i.e., 0.0092 to 0.023/decade), if $\Delta\mu_r$ is taken into account (Figure 10c).

4.2.4. Effect of Gouge Composition (Wet Breccia- Versus Gouge-Derived Samples)

As already shown in section 3.3, the magnitudes ($\Delta\mu_{pk}$) and rates (β_{pk}) of peak healing measured for the wet breccia-derived samples are much higher than the wet gouge-derived samples at otherwise similar conditions (i.e., t_h, T, and V_{SHS}). With reference to Figure 9, this difference is attributed to the fact that the Dieterich components ($\Delta\mu_w$) in the gouge-derived samples are only about one tenth of those for the breccia-derived samples, presumably reflecting their distinct mineralogical composition of the samples. Specifically, the gouge-derived material has abundant phyllosilicate components (35%). It is well known that the presence of phyllosilicates in halite and silicate gouges can significantly inhibit the transient restrengthening processes in the presence of water [*Bos and Spiers*, 2002; *Carpenter et al.*, 2012], due to prevention of contact cementation/healing [*Tesei et al.*, 2012].

Alongside the difference in Dieterich component ($\Delta\mu_w$) between wet gouge- and breccia-derived samples, we note that the magnitudes of $\Delta\mu_r$ for these two sample types are more or less similar (cf. Figures 8a and 8c or Figures 9a and 9b). This means that for the gouge-derived samples, the peak healing observed at hydrothermal conditions (80–140°C) must mostly (~90%) reflect the persistent strengthening effect ($\Delta\mu_r$), whereas for the breccia-derived samples, the contribution by $\Delta\mu_r$ was relatively small ($<20\%$). The quantitive differences in $\Delta\mu_r$ and $\Delta\mu_w$ between these two samples also imply different origins for these two healing components.

4.3. Microphysical Mechanisms Controlling Hydrothermal Healing

In the present experiments, we have observed three types of healing behavior. The mechanisms controlling Type 1a, Dieterich-type healing likely involved static growth or strengthening of solid-solid (grain) contact points during hold periods [*Dieterich*, 1972; *Chen et al.*, 2015], due to indentation creep or diffusive transport. Type 3 healing, characterized by the absence of peak, was seen only in our wet gouge-derived sample sheared at 20°C. According to previous studies that reported similar healing behavior [*Chester and Higgs*, 1992; *Ikari et al.*, 2009; *Tesei et al.*, 2012], this near-zero healing effect may be caused by the saturation of contact area during compaction or hold periods. In the following, we focus on the deformation mechanism(s) responsible for the Type 2 healing.

Type 2 healing, characterized by positive $\Delta\mu_r$, can be seen in the results obtained for both the breccia- and gouge-derived samples tested under hydrothermal conditions. One explanation that can be put forward for the $\Delta\mu_r$ effect after reshearing is the persistence of nonequilibrium pore pressure due to shear-induced dilatation/compaction. However, this cannot account for the observed positive value of $\Delta\mu_r$, because an increase in steady state friction implies lower pore pressure and thus higher porosity, which is inconsistent with the fact that our volumetric data show that progressive compaction occurred during the SHS stages (Figure 12a). A second possibility is that mineral transformation, i.e., smectite-to-illite transformations, may have occurred during the long hold periods. This may explain the enhanced healing seen in the gouge-derived samples but is unlikely to apply to the breccia-derived sample because they contain only 2% clay. A third possibility for explaining the Type 2 healing behavior is strain localization/delocalization [cf. *Sleep et al.*, 2000], which can cause changes in steady state frictional strength by altering the strain rate in the active slip zone. However, the thickness change required by this mechanism makes it again unlikely in our experiments. A simple calculation indicates that a broadening of up to 500 times would be needed to account for the $\Delta\mu_r$ seen in individual SHS events. Against this background, the stepwise increases in steady state friction seen to occur during multistage SHS sequences mean that a Type 2 healing effect due to the combined effects of velocity weakening plus shear band delocalization can be eliminated. Finally, as explained by *Chen et al.* [2015], fluid-assisted deformation mechanisms causing asperity growth/strengthening due to fluid-enhanced indentation creep, or a static increase in cohesion [*Yasuhara et al.*, 2005; *Tenthorey and Cox*, 2006], or else by neck growth [e.g., *Hickman et al.*, 1995; *Niemeijer et al.*, 2008] may explain the Dieterich component of healing ($\Delta\mu_w$) but are unlikely sources of the $\Delta\mu_r$ effect. This is because the enlarged contact area or increased cohesion would be immediately destroyed when reshearing the gouge layer.

4.3.1. Role of Pressure Solution in Wet Experiments

Several lines of evidence indicate that intergranular pressure solution (IPS) likely operated in our wet experiments, especially in the breccia-derived samples. Previous hydrostatic compaction experiments on calcite have shown that IPS is the dominant deformation mechanism in calcite under the *P-T* conditions investigated here [e.g., *X. Zhang et al.*, 2010; *Spiers et al.*, 2004]. The most important evidence for IPS occurring in our wet experiments is the enhanced compaction and shear relaxation creep compared with the dry experiments. First, our thickness measurements on the breccia-derived samples showed much more compaction in the wet samples (~0.31 mm) than in the dry ones (~0.15 mm) (Table 1). Second, real-time compaction was evident from the pore fluid volume change (Figure 12a). Third, hold-time relaxation creep rates are higher for wet breccia-derived samples than for the dry samples at otherwise similar conditions (Figure 13a). Further evidence comes from the sensitivity of compaction and relaxation to temperature during hold periods. As shown in Figures 12b and 13b, both gouge compaction and stress relaxation creep rates exhibit negative dependencies on temperature, from which apparent activation energies can be derived (see Text S2). These fall in the range from -10.8 to -2.4 kJ/mol for compaction, and from -11.1 to -6.9 kJ/mol for shear relaxation creep, consistent with those obtained in hydrostatic experiments on calcite (-29.9 to -9.7 kJ/mol by *X. Zhang et al.* [2010]). Following the arguments given by *Liteanu et al.* [2012], the negative sign is due to the decreasing solubility of calcite with increasing temperature. We have to note, however, that we could not find convincing microstructural evidence for pressure solution in wet breccia-derived samples, although we did find evidence for neck growth and sintering [*Chen et al.*, 2015].

Although the calcite content is lower, we infer that the IPS process was also likely to operate in the wet gouge-derived samples, which consist of almost equal proportions of clay, quartz, and carbonate (mainly dolomite). Previous study has inferred that IPS played a role in controlling the healing behavior of pure quartz gouge at low temperatures [e.g., *Yasuhara et al.*, 2005]. So far, no experimental studies have addressed IPS in dolomite. However, field evidence for IPS, such as stylolites and grain-to-grain sutures, are widespread in dolomitic limestone and dolomite units [e.g., *Wanless*, 1979]. Moreover, data on the dissolution/precipitation kinetic of dolomite suggest that they would not be grossly different from calcite under the present conditions [*Pokrovsky et al.*, 2009]. It seems reasonable to infer then that dolomite may also undergo solution transfer effects similar to calcite in the present experiments on the wet breccia- and gouge-derived samples. On this basis, we infer that the Type 2 healing behavior observed in the wet gouge-derived samples at elevated temperatures is likely attributable to IPS or to surface energy-driven solution transfer processes occurring in both calcite and dolomite, and possibly even in quartz, although solution transfer is known to be very slow in quartz at the present experimental conditions [e.g., *Spiers et al.*, 2004].

The phyllosilicates present in the gouge-derived samples may have a variety of effects on healing involving solution transfer, possibly accelerating interfacial dissolution via surface charge effects or accelerating intergranular diffusion [*Renard et al.*, 2001; *Greene et al.*, 2009; *Kristiansen et al.*, 2011]. On the other hand, clay

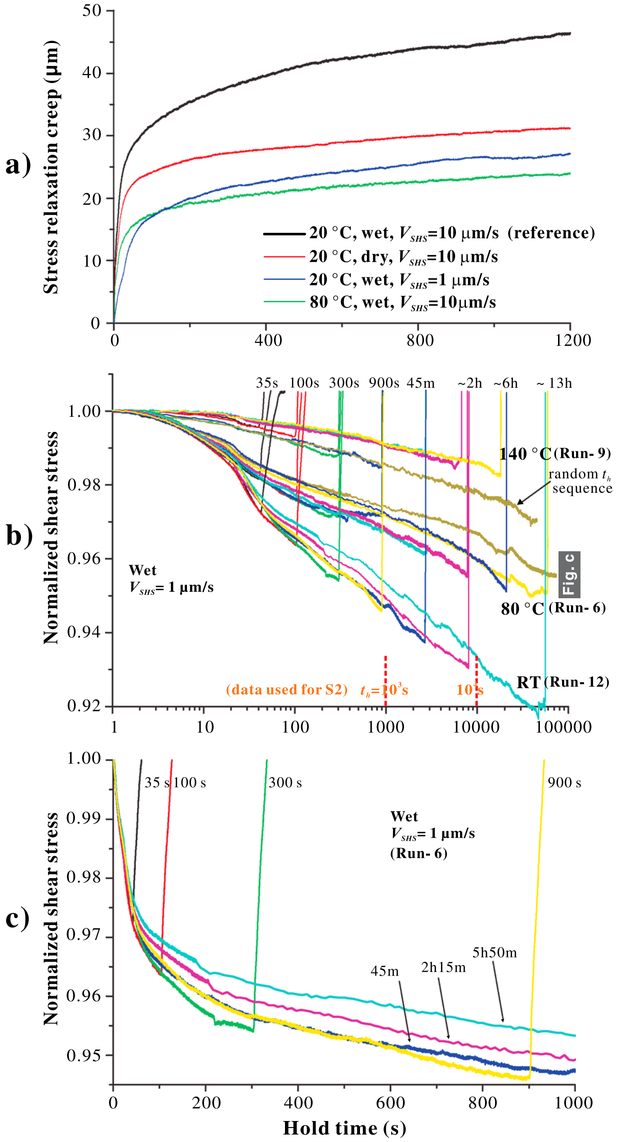

Figure 13. Representative data showing creep displacement and normalized stress relaxation occurring during hold periods in the present experiments on breccia-derived samples. (a) Relaxation creep displacements versus hold time (t_h) for the conditions shown. (b) Normalized stress relaxation versus log(t_h) data from individual SHS tests performed on wet samples at 20, 80, and 140°C, using a SHS velocity of 1 μm/s. (c) Normalized stress relaxation versus t_h data from different SHS events within a single wet experiment performed at 80°C and a SHS velocity of 1 μm/s.

minerals have also been reported to inhibit healing by impeding intergranular neck growth processes, as reported in previous healing studies on salt-clay mixtures [*Bos and Spiers*, 2002]. At the same time, we cannot eliminate the possibility that fluid-assisted subcritical crack growth played a role in the present wet experiments [*Wong and Baud*, 1999]. Hence, it remains difficult to draw firm conclusions on what controls healing in the wet gouges we studied. The main phyllosilicate components contained in our samples (chlorite and mixed smectite-illite) are relatively stable at the temperatures investigated [*Huang et al.*, 1993; *Chen et al.*, 2013b], so that any effects of transformations on healing in our experiments is very unlikely.

As a last piece of evidence, our control experiments (Data Set 4) on breccia-derived samples indicate that fluid chemistry also plays an important role in determining the frictional healing behavior (Figure 11). The use of phosphate solution and silicon oil, both of which inhibit solution transfer in calcite [e.g., *Zhang and Spiers*, 2005], yielded a systematic decrease in the magnitude of stress relaxation ($\Delta\mu_r$) and frictional healing parameters ($\Delta\mu_{pk}$ and $\Delta\mu_w$) in these experiments. Once again, this all points to pressure solution and fluid assisted neck growth or sintering processes contributing to healing in our wet experiments and underscores the role that fluid chemistry may have in controlling healing of natural faults in carbonates.

4.3.2. Physical Origin of $\Delta\mu_r$: Irreversible Compaction

Accepting that pressure solution and/or related processes were likely operative in our wet experiments showing Type 2 behavior, we now consider how IPS could be responsible for the increase in (quasi) steady state frictional strength ($\Delta\mu_r$) observed in our SHS test sequences. As a starting hypothesis in line with the preceding discussion, we propose that positive $\Delta\mu_r$ observed in the SHS sequence of our wet experiments resulted from the increase in contact area due to ongoing, permanent porosity reduction, which was enhanced by the IPS processes. As shown in Figure 12a, the decrease in porosity that occurred during the hold periods did not fully recover to the prehold state during the ongoing reshearing. This implies that reshearing was accommodated in gouge material having persistently lower porosity and/or higher contact cohesion, hence persistently higher strength, than the active gouge zone prior to hold. Note that such an increase in contact area is distinct from the static growth of contact area by indentation creep, which would immediately diminish as slip is reinitiated on contacts, resulting in Type 1a, "Dieterich-type" healing.

To achieve a persistent increase in steady state frictional strength ($\Delta\mu_r$) during posthold reshearing, two possible changes in microstructure can be envisaged. One possibility is permanent widening of the principal boundary shear band upon reshearing (or the formation of a new, wider shear band). This would lead to lower shear band strain rates at a given velocity, and hence to more effective internal competition of compaction, by IPS, versus dilatation associated with cataclastic/granular shear flow. The result would be a lower steady state porosity and higher strength. A second possibility is grain size reduction (i.e., grain breakage) occurring within the principal boundary shear upon posthold reshearing. This too would lead to an enhancement of compaction by IPS relative to dilatation by cataclastic/granular flow, since the rate of IPS compaction increases with decreasing grain size [*X. Zhang*, *et al*., 2010]. We favor this explanation because of the extreme narrowness and submicron grain size of the boundary shear bands seen in our samples [*Chen et al*., 2015; cf. *Verberne et al*., 2013b]. Nonetheless, previous microphysical models, based on gouge deformation by granular flow plus pressure solution, predict increasing steady state friction with both decreasing particle size and with increasing shear band thickness [*Niemeijer and Spiers*, 2007], so that either explanation seems viable.

Therefore, having identified possible origins for the persistent strengthening ($\Delta\mu_r$), we propose that the remaining part of the peak healing ($\Delta\mu_{pk}$) observed in our wet experiments, i.e., $\Delta\mu_w = \Delta\mu_{pk} - \Delta\mu_r$, reflects changes in contact area, resulting from more or less reversible static contact growth and/or strengthening, as envisaged in the Dieterich model for healing. This is supported by the Dieterich-type healing behavior exhibited by $\Delta\mu_w$ in our data (Figures 8 and 9). Hence, our interpretation of $\Delta\mu_{pk}$ observed in our experiments at hydrothermal conditions is that it consists of a Dieterich-type component ($\Delta\mu_w$) related to reversible contact growth and strengthening, plus a non-Dieterich-type component ($\Delta\mu_r$) related to a concomitant irreversible increase in contact area, all enhanced by the operative pressure solution compaction in the shearing band.

4.3.3. Remaining Details of Frictional Healing Data

Reexamining the details of our SHS data, we find that all aspects of the healing behavior seen in the wet experiments at 20–140°C can be explained by the "irreversible compaction" mechanism put forward above. The fact that the shear relaxation creep was faster in early hold periods than in the later periods (Figure 13c) can be explained by a smaller contact area (corresponding to higher porosity) that supported the applied shear stress in the early holds. In the control experiments performed with cycled hold time sequences (Runs 2 and 4, Table 1), $\Delta\mu_c$ and $\Delta\mu_r$ measured in the increasing hold time sequence were much larger than in the subsequent decreasing sequence for the same hold times (Figure 11d). This is consistent with the rate of IPS being smaller in the decreasing sequence owing to lower porosity. Similar reasoning can also apply to the testing run with random hold times (Run 9, Table 1), in which the early long hold yielded an abnormally large $\Delta\mu_c$ and $\Delta\mu_r$ effects (Figures 7c and 8c).

4.4. Implications for Natural Earthquakes

4.4.1. Implications for Seismicity in Tectonically Active Carbonate Terrains

The present experiments on carbonate fault rocks indicate that standard concepts of frictional healing, as embodied in the RSF laws [*Dieterich*, 1972], need to be modified to describe healing under hydrothermal conditions. In our wet experiments on both samples studied here, we observed a positive temperature dependence of transient frictional healing ($\Delta\mu_{pk}$) and a persistent strengthening effect ($\Delta\mu_r$) at elevated temperatures. The latter effect did not occur in the dry experiments. Our interpretation for carbonate faults is that estimates of healing made by extrapolating dry, room temperature results may significantly underestimate both the magnitudes and rates of fault healing that apply to in situ hydrothermal conditions, where thermally and chemically activated processes are expected to be active, leading to marked restrengthening of natural faults during interseismic periods [cf. *Nakatani and Scholz*, 2004].

In particular, our results demonstrate that the gouge-derived sample subjected to hydrothermal conditions ($T > 80$°C) can heal at relatively high healing rates (β_{pk}) up to 0.0068/decade. This value is much larger than the rates (<0.002/decade) typically seen in room temperature results for phyllosilicate/calcite gouges [*Tesei et al*., 2012]. Recent room temperature experiments have yielded zero or even negative healing rates for natural gouge materials collected from tectonically active faults, such as the San Andreas Fault [*Carpenter et al*., 2012], the Alpine Fault [*Boulton et al*., 2012], and here the LFZ (Figure 8a). This means that healing properties of upper crustal faults often thought to deform predominantly by aseismic creep of phyllosilicate-rich gouge need to be (re)examined via experiments conducted at in situ conditions.

Our results provide new experimental insights for understanding the dynamics of earthquake on active faults in carbonate terrains, such as the Apennines, Italy [e.g., *Verberne et al*., 2010; *Collettini et al*., 2014; *Scuderi et al*., 2013; *Bullock et al*., 2014; *Carpenter et al*., 2014]. For both dry and wet breccia-derived samples, we revealed a transition in velocity dependence of friction from positive to negative with increasing temperature (depth), specifically at about 80°C. Our results further showed that after sequential healing stages involved in our experiments, this transition will shift to higher temperatures, resulting a negative $(a - b)$ being first seen at 140°C (Figure 5). Assuming a geothermal gradient of 20°C/km, the temperature of 140°C suggests the onset of velocity weakening and thus possible seismogenesis at depth of ~7 km. At these depths ($>$7 km), the phyllosilicate content of carbonate faults is expected to be low, and the carbonate content high, as it is only at shallow levels ($<$5 km) that fault zone porosity and permeability will be high enough to allow carbonate dissolution/removal and phyllosilicate concentration, as demonstrated by *Chen et al*. [2013a]. Moreover, from others' work elsewhere [e.g., *Collettini et al*., 2014; *Fondriest et al*., 2012], and from our own observation on fault scarps within the LFZ, it is well established that carbonate faults exhumed from depth are generally dominated by (cemented) cataclasite and ultracataclasite and do not usually show phyllosilicate-rich cores. Therefore, these results can be expected to apply to the fault rocks present at depths greater than 7 km on fault in carbonate terrains. In addition, our results for wet, carbonate/clay-rich samples suggest that shallower fault segments where a clay-rich gouge has developed will always be characterized by velocity-strengthening behavior (Figure 5a). On the other hand, the enhanced healing effects reported here, in both clay-rich and clay-poor gouges, suggest relatively easy and rapid development of earthquake asperities within the shallow portions of faults in carbonate terrains where large aftershocks often occur ($M_L > 4$ at ~2 km [*Chiarabba et al*., 2009]).

Another key observation in this present study is that under hydrothermal conditions, which probably represent the in situ hydrological state of natural faults at depths, a hold stage imposed between periods at stepped velocities, i.e., a simulated interseismic healing period, can cause an increase in $(a - b)$ (Figure 5). As demonstrated by control experiments Run 17 and Run 11, which involved pure velocity stepping (Run 17, Figure 11e) and a single long hold between two VS sequences (Run 11, Figure 11f), this "stabilization effect" is unlikely to be due to accumulated displacement. The implication is that interseismic frictional healing may stabilize rupture nucleation in carbonate-rich faults. If this is applicable to active fault, during long-term interseismic healing periods, this stabilization effect should result in the upper limit of the seismogenic zone tending to migrate to deeper crustal levels. In principle, this effect, combined with the enhanced healing effects described above, will tend to promote the nucleation of deeper earthquakes with increasing magnitude. However, we can find no evidence in natural earthquake records to support the existence of such effects. This absence of such evidence may, of course, reflect preferred operation of other processes, such as initiation/activation of new, weaker fault planes as healing strengthens shallow fault segments [e.g., *Hou et al*., 2012; *Bullock et al*., 2014] or else broadening of the original fault zone as deformation spreads into weaker marginal regions of the fault [e.g., *Collettini et al*., 2014].

4.4.2. Implications for the LFZ (the Wenchuan Earthquake Fault)

With respect to the Wenchuan earthquake, two principal asperity regions were associated with the main shock [*Zhang et al*., 2009]. One lies the vicinity of the hypocenter, which is inferred to be related to the Precambrian Pengguan complex (metavolcanic and metaintrusive rocks), and the other is ~100 km north [*Wang et al*., 2011], a region where the coseismic rupture cut through extensive carbonate rocks [*Chen et al*., 2013a; *Cao et al*., 2011]. The exposure studied here falls into the latter region. On the basis of geophysical inversion results [*Zhang et al*., 2009; *Zhao et al*., 2010], coseismic slip in this carbonate region predominantly occurred in the upper 10 km. High-precision relocation studies showed that strong aftershocks occurred in this area, characterized by magnitudes up to M_s 5.2 and focal depths of ~10 km [*Zhang et al*., 2008; *Jia et al*., 2010]. Deep gas wells drilled in this area showed that carbonates dominate down to at least 7560 m [*Cao et al*., 2011]. Seismic reflection profiles further revealed that the sedimentary strata persist down to at least 9 km [*Jia et al*., 2010]. All these pieces of evidence suggest that the extensive carbonate sequences seen at the surface are probably present at depth where rupture nucleated and anyway hosted most of the trajectory followed by the rupture process. Against this background, our present study offers relevant constraints on faulting dynamics in the carbonate cover affected by the Wenchuan earthquake rupture. We consider these cautiously below.

First, we have reported on high healing rates (β_{pk}) for carbonate breccia (up to 0.023/decade). The values obtained are higher than the healing rates reported for most other rock types (see a compilation by

Renard et al. [2012]). Moreover, carbonate rocks are also strong, displaying a friction coefficient of typically ~0.7 (Table 1). The combined effects are consistent with the carbonate rocks present in the sampled segment of the LFZ at least contributing to the asperity associated with the Wenchuan earthquake on the northern part of the LFZ.

Second, as already discussed, our wet breccia-derived samples showed a transition from velocity-strengthening to velocity-weakening slip at 80°C. After a cumulative hold time of ~24 h in our experiments, velocity weakening was first seen at ~140°C, corresponding to depths greater than 7 km. Our results is thus consistent with available data from the Wenchuan earthquake, which suggests a focal depth of about 10 km [*Zhang et al.*, 2008], after a period without large earthquakes of at least 2700 years [*P. Zhang et al.*, 2010].

Third, we have found a positive dependence of $(a-b)$ on sliding velocity, with a sensitivity of 0.001–0.0035 per decade change in velocity (Figure 6). On basis of this, we can crudely extrapolate the $(a-b)$ values obtained in our experiments for slip rates of 0.1–10 μm/s to long-term slip rates in natural fault. Taking the breccia sample which has a $(a-b)$ value of -0.004 at 140°C and slip rate of 1 μm/s (Figure 6c), this yields $(a-b)$ values falling in the range from -0.01 to -0.02 for the displacement rate of no more than 1 mm/yr on the LFZ prior to the Wenchuan earthquake [*P. Zhang et al.*, 2010]. These values are more negative than the values reported for other rock types that show velocity-weakening behavior (>-0.009; see a compiled data set by *Paterson and Wong* [2005]), suggesting significant potential for slip instability [cf. *Wong and Zhao*, 1990; *Beeler et al.*, 2001]. At the same time, however, caution must be exercised when applying the laboratory-derived “seismicity criteria” to slowly driven, long-reoccurrence faults, such as the LFZ [*Zhang*, 2013].

4.5. Broader Comparison With Previous Work

Finally, we consider previous results that show behavior similar to the Type 2 healing behavior reported here ($\Delta\mu_r > 0$), and we assess if the healing parameters we have defined (Figure 2b) and the healing partitioning we have observed (Figure 9) in the present study apply to these previous data.

We found three studies in literature that can be used. Two are on quartz gouges sheared at hydrothermal conditions [*Nakatani and Scholz*, 2004; *Yasuhara et al.*, 2005], and the other is on wet gypsum sheared at room temperature [*Muhuri et al.*, 2003]. In all these studies, pressure solution was inferred to be the mechanism responsible for the enhanced strengthening observed. As presented in Figure 14, the SHS results obtained in these studies exhibited restrengthening effects in both the transient peak and steady state frictional strengths. These feature were absent in the authors’ wet, cold, and dry experiments. We applied our healing partitioning concept (Figure 9) to these previous data. Generally speaking, the “direct” healing values $\Delta\mu$ (or $\Delta\mu_{pk}$ in our definition), picked from the original data, are scattered and do not indicate clear linear relations with $\log(t_h)$ (Figure 14). However, after subtracting $\Delta\mu_r$, the residual portion ($\Delta\mu_w = \Delta\mu_{pk} - \Delta\mu_r$) for all three data sets yield a systematic linear relationship with the logarithm of hold time. As a specific example, *Muhuri et al.* [2003] performed SHS tests with hold times administered first in an increasing sequence and then a decreasing one. They observed a marked $\Delta\mu_r$ effect in the first sequence and a minor effect in the reverse sequence. However, “$\Delta\mu_w$” data derived from the two sequences are consistent with one another and show a log linear relation versus hold time (Figure 14c). These features are exactly as analogous with what we observed in our runs with increasing and decreasing hold times (Figure 11d).

Several other experiments also show increases in steady state friction (positive $\Delta\mu_r$). *Fredrich and Evans* [1992], *Karner et al.* [1997], and *Tenthorey and Cox* [2006] performed so-called “hold-slide” experiments on quartz gouges at hydrothermal conditions and observed strengthening in both peak and steady state friction. However, in these experiments, the gouges were “healed” at high temperature (636°C) prior to sliding at 200°C. The strengthening observed accordingly reflected the effects of lithification at high temperature by mineral precipitation, which was inferred to be different from the mechanism(s) operated during sliding.

Lastly, “reduced-stress” SHS experiments performed at dry, room temperature have shown that decreasing the shear stress during the hold periods can lead to an increase in dynamic friction and hence in peak friction upon resliding [*Nakatani and Mochizuki*, 1996; *Karner and Marone*, 2001]. As evidenced by strong compaction observed in the hold periods [*Marone and Scholz*, 1989], the underlying mechanism for enhanced healing in these experiments was attributed to “tight packing” of the gouge due to particle

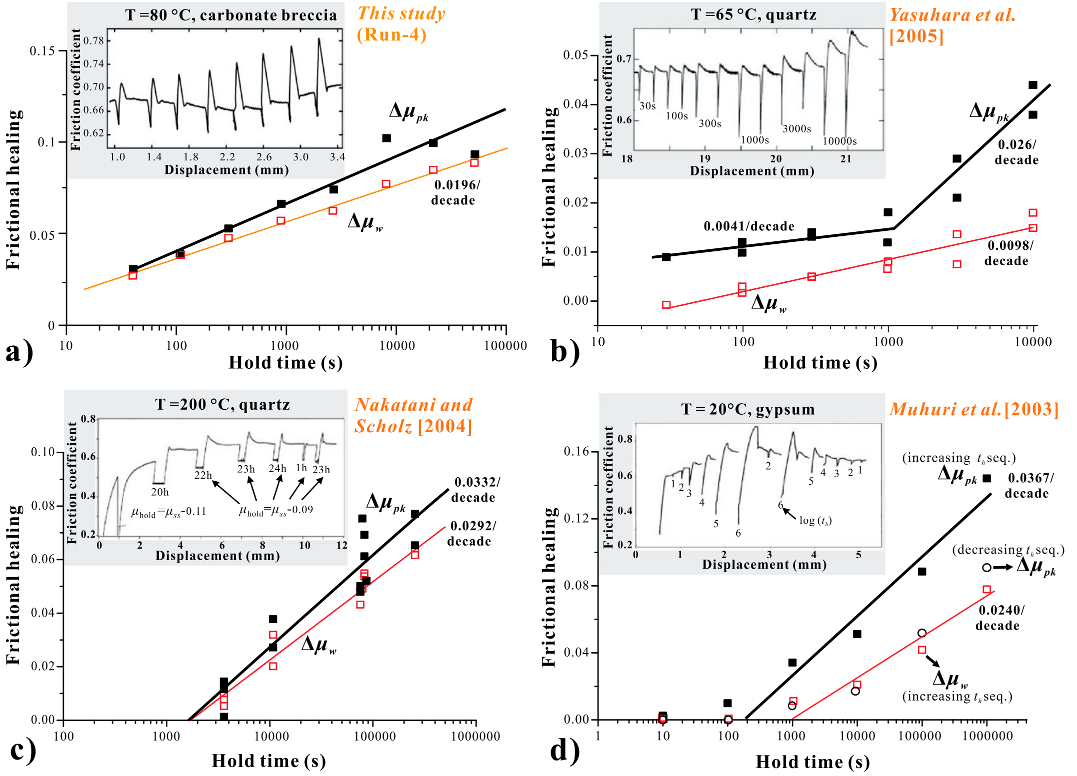

Figure 14. Comparison between (a) a representative frictional healing experiment on wet carbonate breccia sample, with previous experiments on (b and c) wet quartz and on (d) wet gypsum gouges. The inset graphs in Figures 14b–14d present the friction versus displacement results as given in Figure 2b of *Yasuhara et al.* [2005], in Figure 1a of *Nakatani and Scholz* [2004], and in Figure 1a of *Muhuri et al.* [2003], respectively. The frictional healing data presented ($\Delta\mu_{pk}$ and $\Delta\mu_w$) are derived from the "raw data" from these experiments using the definition (Figure 2b) and healing partitioning approach (Figure 9) developed in this study. In Figure 14b, the data points representing $\Delta\mu_{pk}$ are relatively scattered and exhibit a change in slope with respect to log(t_h), with healing rates being shown separately for different intervals. However, the $\Delta\mu_w$ data obtained by subtracting $\Delta\mu_r$ from $\Delta\mu_{pk}$ converge together to yield a linear relation of $\Delta\mu_w$ versus log(t_h). In Figure 14c, after subtracting $\Delta\mu_r$ from $\Delta\mu_{pk}$, the $\Delta\mu_w$ data become less scattered compared with $\Delta\mu_{pk}$ and indicate more clearly a Dieterich-type healing behavior. In Figure 14d, the SHS tests were performed in first an increasing t_h sequence followed by the reverse sequence. The $\Delta\mu_{pk}$ data obtained in these two sequences deviate from one another. However, after subtracting $\Delta\mu_r$, the two sets of $\Delta\mu_w$ data converge together and show a log linear relation versus hold time.

rearrangement when reducing the shear stress. This tightening-up effect is to some extent similar to the irreversible compaction observed in our wet experiments, although the deformation mechanisms are different.

By making a broad comparison with these previous results, we conclude that (1) our observations of Type 2 healing behavior are not restricted to carbonate (-rich) rocks but may apply to a wide variety of rock types; (2) it can be expected to occur preferentially under hydrothermal conditions where fluid-transfer processes are active; and (3) in general, any deformation mechanism that facilitates "irreversible compaction" of active shear bands can help produce this behavior. All these previously proposed mechanisms, i.e., "pressure solution" [*Muhuri et al.*, 2003], "enhanced lithification" [*Karner et al.*, 1997], and "tight packing" [*Nakatani and Mochizuki*, 1996], can to some extent lead to irreversible compaction of shear bands during the hold periods. In this point of view, these mechanisms can be classified into a general class of healing mechanism ($\Delta\mu_r$ effect) not according to the specific microscopic processes but according to the structures altered by whatever process.

5. Conclusions

We have reported direct shear friction experiments on simulated gouges prepared from carbonate (-rich) fault rocks collected from the LFZ, Sichuan, China. Samples consisted of (i) a carbonate-dominated breccia and (ii) a carbonate/clay-rich fault core-derived gouge. Our experiments were conducted dry, and under hydrothermal conditions, at temperatures ranging from 20 to 140°C, at an effective normal stress of 50 MPa, involving a VS stage, a SHS stage, and a second VS stage. We measured the friction rate dependence and healing parameters, exploring the effects of temperature, sliding rate, and hold times. The following conclusions can be drawn:

1. We found distinct frictional strengths for dry and wet breccia-derived samples ($\mu = 0.64$–0.72) versus for the wet gouge-derived samples ($\mu = 0.30$–0.34). All sample types tested showed a decrease of $(a - b)$ with increasing temperature. Dry and wet breccia-derived samples not subjected to healing displayed a transition from velocity strengthening to velocity weakening at ~80°C, while wet gouge-derived samples showed velocity-strengthening slip at all temperatures investigated.
2. SHS tests on the dry breccia-derived samples showed Dieterich-type healing behavior, characterized by a log linear relation between peak healing ($\Delta\mu_{pk}$) versus hold time. However, in the SHS tests performed under hydrothermal conditions, both the gouge- and breccia-derived samples showed "non-Dieterich-type" healing behavior, characterized by a persistent increase in (quasi) steady state friction coefficient ($\Delta\mu_r > 0$) after the hold period. The peak healing ($\Delta\mu_{pk}$) observed in our hydrothermal experiments consists of two components, i.e., a postpeak drop (the $\Delta\mu_w$ effect) plus the $\Delta\mu_r$ effect.
3. Frictional healing rates of the dry breccia-derived samples increase with increasing temperature, consistent with previously published data from dry or wet friction tests on quartz and feldspar. At the same time, the wet breccia-derived samples showed larger healing rates (β_{pk}) and with a more complex dependence of β_{pk} on temperature. By contrast, wet gouge-derived samples show an increase in peak healing rate β_{pk} by ~10 times, from 0.0006/decade at 20°C to 0.0059/decade at 140°C.
4. Mechanisms that are previously proposed to explain Dieterich-type healing (e.g., indentation creep and neck growth) cannot explain the persistent increase of steady state friction, i.e., $\Delta\mu_r > 0$, as observed in our wet experiments. We infer that this is related to permanent, progressive porosity reduction during hold periods due to intergranular pressure solution.
5. Repeated healing of our samples under hydrothermal conditions led to an increase in $(a - b)$ or slip "stabilization." When extrapolated to natural faults in tectonically active carbonate terrains, this implies that interseismic frictional healing may alter the seismogenic potential of a fault cutting carbonate rocks, resulting in the migration of the upper limit of the seismogenic zone to deeper crustal levels.
6. Our results imply that when fluid-assisted processes are an important healing mechanism, applying a log linear trend will underestimate natural fault healing and that quantitative models must account for fluid-assisted processes as inferred here. In particular, carbonate/clay-rich fault rocks, as seen in LFZ, can heal at rates much higher than previously recognized from room temperature experiments.

Acknowledgments

We would like to thank Peter van Krieken and Gert Kastelein for their technical support in maintaining the testing machine. J.C. was funded by China NSF (41372202), the Basic Scientific Funding of Chinese National Nonprofit Institutes (IGCEA1405), the China NSF (41102130), and by the Netherlands Center for Solid Earth Science (ISES) grant 2013-103, while B.A. V. was supported by ISES grant 2011-75. We thank K. Oohashi, an anonymous reviewer, and the Associate Editor for their review and positive feedback on this paper. All the experimental data for this paper are freely available through http://pan.baidu.com/s/1bnhLa95, and testing materials to reproduce the experiments are available from the authors upon request (jychen@ies.ac.cn).

References

Baumberger, T., P. Berthoud, and C. Caroli (1999), Physical analysis of state- and rate-dependent friction law, II. Dynamic friction, *Phys. Rev. B.*, *60*(6), 3928–3939.

Beeler, N. M., S. H. Hickman, and T.-F. Wong (2001), Earthquake stress drop and laboratory-inferred interseismic strength recovery, *J. Geophys. Res.*, *106*, 30,371–30,713, doi:10.1029/2000JA001101.

Bernard, J. E., W. Hubert, and M. Diraison (2006), Seismicity wedge beneath the Upper Rhine Graben due to backwards Alpine push?, *Tectonophysics*, *428*, 49–64.

Blanpied, M. L., D. A. Lockner, and J. D. Byerlee (1995), Frictional slip of granite at hydrothermal conditions, *J. Geophys. Res.*, *100*, 13,045–13,064, doi:10.1029/95JB00862.

Bos, B., and C. J. Spiers (2002), Fluid-assisted healing processes in gouge bearing faults: Insights from experiments on a rock analogue system, *Pure Appl. Geophys.*, *159*, 2537–2566.

Boulton, C., B. M. Carpenter, V. Toy, and C. Marone (2012), Physical properties of surface outcrop cataclastic fault rocks, Alpine Fault, New Zealand, *Geochem. Geophys. Geosyst.*, *13*, Q01018, doi:10.1029/2011GC003872.

Bréchet, Y., and Y. Estrin (1994), The effect of strain rate sensitivity on dynamic friction of metals, *Scr. Metall. Mater.*, *30*, 1449–1454.

Bullock, R. J., N. De Paola, R. E. Holdsworth, and J. Trabucho-Alexandre (2014), Lithological controls on the deformation mechanisms operating within carbonate-hosted faults during the seismic cycle, *J. Struct. Geol.*, *58*, 22–42.

Byerlee, J. D. (1978), Friction of rocks, *Pure Appl. Geophys.*, *116*, 615–626.

Cao, J. X., S. G. Liu, R. F. Tian, X. J. Wang, and X. Y. He (2011), Seismic prediction of carbonate reservoirs in the deep of Longmenshan foreland basin [in Chinese with English abstract], *Acta Petrol. Sin.*, *27*(8), 2423–2434.

Carpenter, B. M., D. M. Saffer, and C. Marone (2012), Frictional properties and sliding stability of the San Andreas Fault from deep drill core, *Geology*, *40*(8), 759–762, doi:10.1130/G33007.1.

Carpenter, B. M., M. M. Scuderi, C. Collettini, and C. Marone (2014), Frictional heterogeneities on carbonate-bearing normal faults: Insights from the Monte Maggio Fault, Italy, *J. Geophys. Res. Solid Earth*, *119*, 9062–9076, doi:10.1002/2014JB011337.

Chen, J., X. Yang, S. Ma, and C. J. Spiers (2013a), Mass removal and clay mineral dehydration/rehydration in carbonate-rich surface exposures of the 2008 Wenchuan earthquake fault: Geochemical evidence and implications for fault zone evolution and coseismic slip, *J. Geophys. Res. Solid Earth*, *118*, 474–496, doi:10.1002/jgrb.50089.

Chen, J., X. Yang, Q. Duan, T. Shimamoto, and C. J. Spiers (2013b), Importance of thermochemical pressurization in the dynamic weakening of the Longmenshan Fault during the 2008 Wenchuan earthquake: Inferences from experiments and modeling, *J. Geophys. Res. Solid Earth*, *118*, 4145–4169, doi:10.1002/jgrb.50260.

Chen, J., B. A. Verberne, and C. J. Spiers (2015), Interseismic re-strengthening and stabilization of carbonate faults by "non-Dieterich" healing under hydrothermal conditions, *Earth Planet. Sci. Lett.*, *423*, 1–12, doi:10.1016/j.epsl.2015.03.044.

Chester, F. M., and N. G. Higgs (1992), Multimechanism friction constitutive model for ultrafine quartz gouge at hypocentral conditions, *J. Geophys. Res.*, *97*, 1859–1870, doi:10.1029/91JB02349.

Chiarabba, C., et al. (2009), The 2009 L'Aquila (central Italy) M_w 6.3 earthquake: Main shock and aftershocks, *Geophys. Res. Lett.*, *36*, L18308, doi:10.1029/2009GL039627.

Collettini, C., B. M. Carpenter, C. Viti, F. Cruciani, S. Mollo, T. Tesei, F. Trippetta, L. Valoroso, and L. Chiaraluce (2014), Fault structure and slip localization in carbonate-bearing normal faults: An example from the northern Apennines of Italy, *J. Struct. Geol.*, *67*, 154–166.

De Jong, S. M., C. J. Spiers, and A. Busch (2014), Development of swelling strain in smectite clays through exposure to carbon dioxide, *Int. J. Greenhouse Gas Control*, *24*, 149–161.

Den Hartog, S. A. M., A. R. Niemeijer, and C. J. Spiers (2013), Friction on subduction megathrust faults: Beyond the illite-muscovite transition, *Earth Planet. Sci. Lett.*, *373*, 8–19.

Dieterich, J. H. (1972), Time-dependent friction in rocks, *J. Geophys. Res.*, *77*, 3690–3697, doi:10.1029/JB077i020p03690.

Drennon, C. B., and R. L. Handy (1972), Stick-slip of lightly loaded limestone, *Int. J. Rock Mech. Min. Sci.*, *9*, 603–615.

Fondriest, M., S. A. F. Smith, G. Di Toro, D. Zampier, and S. Mittempergher (2012), Fault zone structure and seismic slip localization in dolostone, an example from the southern Alps, Italy, *J. Struct. Geol.*, *45*, 52–67.

Fredrich, J. T., and B. Evans (1992), Strength recovery along simulated faults by solution transfer, Proc. U.S, *Rock Mech. Symp.*, *33*, 121–130.

Greene, G. W., K. Kristiansen, E. E. Meyer, J. R. Boles, and J. N. Israelachvili (2009), Role of electrochemical reactions acceptedure solution, *Geochim. Cosmochim. Acta*, *73*, 2862–2874.

Han, R., T. Shimamoto, T. Hirose, J. Ree, and J. Ando (2007), Ultralow friction of carbonate faults caused by thermal decomposition, *Science*, *316*, 878–881.

He, C., Z. Wang, and W. Yao (2007), Frictional sliding of gabbro gouge under hydrothermal conditions, *Tectonophysics*, *445*, 353–362.

Hickman, S., R. Sibson, and R. Bruhn (1995), Introduction to special section: Mechanical involvement of fluids in faulting, *J. Geophys. Res.*, *100*, 12,831–12,840, doi:10.1029/95JB01121.

Hou, L., S. Ma, T. Shimamoto, J. Chen, J. Yao, X. Yang, and Y. Okimura (2012), Internal structures and high-velocity frictional properties of a bedding-parallel carbonate fault at Xiaojiaqiao outcrop activated by the 2008 Wenchuan earthquake, *Earthquake Sci.*, *25*, 197–217.

Huang, W. L., J. M. Longo, and D. R. Pevear (1993), An experimentally derived kinetic model for smectite-to-illite conversion and its use as a geothermometer, *Clays Clay Miner.*, *41*, 162–177.

Ikari, M. J., D. M. Saffer, and C. Marone (2009), Frictional and hydrologic properties of clay-rich fault gouge, *J. Geophys. Res.*, *114*, B05409, doi:10.1029/2008JB006089.

Jia, D., Y. Li, A. Lin, M. Wang, W. Chen, X. Wu, Z. Ren, Y. Zhao, and L. Luo (2010), Structural model of 2008 M_w 7.9 Wenchuan earthquake in the rejuvenated Longmen Shan thrust belt, China, *Tectonophysics*, *491*, 174–184.

Karner, S. L., and C. Marone (2001), Frictional restrengthening in simulated fault gouge: Effect of shear load perturbations, *J. Geophys. Res.*, *106*, 19,319–19,337, doi:10.1029/2001JB000263.

Karner, S. L., C. Marone, and B. Evans (1997), Laboratory study of fault healing and lithification in simulated fault gouge under hydrothermal conditions, *Tectonophysics*, *277*, 41–55.

Kristiansen, K., M. Valtiner, G. W. Greene, J. R. Boles, and J. N. Israelachvili (2011), Pressure solution—The importance of the electrochemical surface potentials, *Geochim. Cosmochim. Acta*, *75*, 6882–6892.

Li, Y.-G., J. E. Vidale, S. M. Day, D. D. Oglesby, and E. Cochran (2003), Postseismic fault healing on the rupture zone of the 1999 *M* 7.1 Hector Mine, California, earthquake, *Bull. Seismol. Soc. Am.*, *93*, 854–869.

Liteanu, E., A. Niemeijer, C. J. Spiers, C. J. Peach, and J. H. P. de Bresser (2012), The effect of CO_2 on creep of wet calcite aggregates, *J. Geophys. Res.*, *117*, B03211, doi:10.1029/2011JB008789.

Liu, J., J. M. Walter, and K. Weber (2002), Fluid-enhanced low-temperature plasticity of calcite marble: Microstructures and mechanisms, *Geology*, *30*(9), 787–790.

Marone, C. (1998a), Laboratory-derived friction laws and their application to seismic faulting, *Annu. Rev. Earth Planet. Sci.*, *26*, 643–696, doi:10.1146/annurev.earth.26.1.643.

Marone, C. (1998b), The effect of loading rate on static friction and the rate of fault healing during the earthquake cycle, *Nature*, *391*, 69–72.

Marone, C., and D. M. Saffer (2015), The mechanics of frictional healing and slip instability during the seismic cycle, in *Treatise on Geophysics*, edited by H. Kanamori et al., 2nd ed., pp. 111–138, Elsevier, Oxford, U. K.

Marone, C., and C. H. Scholz (1989), Particle-size distribution and microstructures within simulated fault gouge, *J. Struct. Geol.*, *11*(7), 799–814.

Marone, C., J. E. Vidale, and W. Ellsworth (1995), Fault healing inferred from time dependent variations in source properties of repeating earthquakes, *Geophys. Res. Lett.*, *22*, 3095–98, doi:10.1029/95GL03076.

Mitchell, E. K., Y. Fialko, and K. M. Brown (2012), Temperature dependence of frictional healing of westerly granite: Experimental observations and numerical simulations, *Geochem. Geophys. Geosyst.*, *14*, 567–582, doi:10.1029/2012GC004241.

Mizoguchi, K., T. Hirose, T. Shimamoto, and E. Fukuyama (2008), Internal structure and permeability of the Nojima Fault, southwest Japan, *J. Struct. Geol.*, *30*, 513–524.

Morrow, C., B. Radney, and J. Byerlee (1992), Frictional strength and the effective pressure law of montmorillonite and illite clays, in *Fault Mechanics and Transport Properties of Rocks*, *Int. Geophys. Ser.*, vol. 51, edited by B. Evans and T.-F. Wong, pp. 69–88, Academic Press, London.

Muhuri, S. K., T. A. Dewers, T. E. Scott Jr., and Z. Reches (2003), Interseismic fault strengthening and earthquake-slip instability: Friction or cohesion?, *Geology*, *31*, 881–884, doi:10.1130/G19601.1.

Nakatani, M. (2001), Conceptual and physical clarification of rate and state friction: Frictional sliding as a thermally activated rheology, *J. Geophys. Res.*, *106*, 13,347–13,380, doi:10.1029/2000JB900453.

Nakatani, M., and H. Mochizuki (1996), Effects of shear stress applied to surfaces in stationary contact on rock friction, *Geophys. Res. Lett.*, *23*, 869–872, doi:10.1029/96GL00726.

Nakatani, M., and C. H. Scholz (2004), Frictional healing of quartz gouge under hydrothermal conditions: 1. Experimental evidence for solution transfer healing mechanism, *J. Geophys. Res.*, *109*, B07201, doi:10.1029/2001JB001522.

Niemeijer, A. R., and C. J. Spiers (2007), A microphysical model for strong velocity weakening in phyllosilicate-bearing fault gouges, *J. Geophys. Res.*, *112*, B10405, doi:10.1029/2007JB005008.

Niemeijer, A., C. Marone, and D. Elsworth (2008), Healing of simulated fault gouges aided by pressure solution: Results from rock analogue experiments, *J. Geophys. Res.*, *113*, B04204, doi:10.1029/2007JB005376.

Olsson, W. A. (1974), Effect of temperature, pressure and displacement rate on the frictional characteristics of a limestone, *Int. J. Rock Mech. Min. Sci. Geomech. Abstr*, *11*, 267–278.

Paterson, M. S., and T.-F. Wong (2005), *Experimental Rock Deformation—The Brittle Field*, 2nd ed., Springer, Berlin.

Pokrovsky, O. S., S. V. Golubev, J. Schott, and A. Castillo (2009), Calcite, dolomite and magnesite dissolution kinetics in aqueous solutions at acid to circumneutral pH, 25 to 150°C and 1 to 55 atm $p\mathrm{CO_2}$: New constraints on $\mathrm{CO_2}$ sequestration in sedimentary basins, *Chem. Geol.*, *265*, 20–32.

Renard, F., D. Dysthe, J. Feder, K. Bjorlykke, and B. Jamtveit (2001), Enhanced pressure solution creep rates induced by clay particles: Experimental evidence in salt aggregates, *Geophys. Res. Lett.*, *28*, 1295–1298, doi:10.1029/2000GL012394.

Renard, F., S. Beauprêtre, C. Voisin, D. Zigone, T. Candela, D. K. Dysthe, and J.-P. Gratier (2012), Strength evolution of active frictional interface is controlled by the dynamics of contacts and chemical effects, *Earth Planet. Sci. Lett.*, *341–344*, 20–34.

Ruina, A. (1983), Slip instability and state variable friction laws, *J. Geophys. Res.*, *88*, 10,359–10,370, doi:10.1029/JB088iB12p10359.

Rutter, E. H., and D. H. Mainprice (1978), The effect of water on the stress relaxation of faulted and unfaulted sandstone, *Pure Appl. Geophys.*, *116*, 634–54.

Samuelson, J., and C. J. Spiers (2012), Fault friction and slip stability not affected by $\mathrm{CO_2}$ storage: Evidence from short-term laboratory experiments on North Sea reservoir sandstones and caprocks, *Int. J. Greenhouse Gas Control*, *11*, S78–S90.

Scholz, C. H. (2002), *The Mechanics of Earthquakes and Faulting*, 2nd ed., 471 pp., Cambridge Univ. Press, New York.

Scuderi, M. M., A. R. Niemeijer, C. Collettini, and C. Marone (2013), Frictional properties and slip stability of active faults within carbonate–evaporate sequences: The role of dolomite and anhydrite, *Earth Planet. Sci. Lett.*, *369–370*, 220–232.

Sibson, R. H. (1982), Fault zone models, heat flow, and the depth distribution of earthquakes in the continental crust of the United States, *Bull. Seismol. Soc. Am.*, *72*(1), 151–163.

Sleep, N. H., E. Richardson, and C. Marone (2000), Physics of strain localization in synthetic fault gouge, *J. Geophys. Res.*, *105*, 25,875–25,890, doi:10.1029/2000JB900288.

Spiers, C. J., S. De Meer, A. R. Niemeijer, and X. Zhang (2004), Kinetics of rock deformation by pressure solution and the role of thin aqueous films, in *Physicochemistry of Water in Geological and Biological Systems*, edited by S. Nakashima et al., pp. 129–158, Univ. Acad. Press, Tokyo.

Tembe, S., D. A. Lockner, and T.-F. Wong (2010), Effect of clay content and mineralogy on frictional sliding behavior of simulated gouges: Binary and ternary mixtures of quartz, illite, and montmorillonite, *J. Geophys. Res.*, *115*, B03416, doi:10.1029/2009JB006383.

Tenthorey, E., and S. F. Cox (2006), Cohesive strengthening of fault zones during the interseismic period: An experimental study, *J. Geophys. Res.*, *111*, B09202, doi:10.1029/2005JB004122.

Tesei, T., C. Collettini, B. M. Carpenter, C. Viti, and C. Marone (2012), Frictional strength and healing behavior of phyllosilicate-rich faults, *J. Geophys. Res.*, *117*, B09402, doi:10.1029/2012JB009204.

Verberne, B. A., C. He, and C. J. Spiers (2010), Frictional properties of sedimentary rocks and natural fault gouge from the Longmenshan Fault Zone, Sichuan, China, *Bull. Seismol. Soc. Am.*, *100*, 2767–2790.

Verberne, B. A., J. H. P. De Bresser, A. R. Niemeijer, C. J. Spiers, D. A. M. De Winter, and O. Plümper (2013a), Nanocrystalline slip zones in calcite fault gouge show intense crystallographic preferred orientation: Crystal plasticity at subseismic slip rates at 18–150°C, *Geology*, *41*, 863–866.

Verberne, B. A., C. J. Spiers, A. R. Niemeijer, J. H. P. De Bresser, D. A. M. De Winter, and O. Plümper (2013b), Frictional properties and microstructure of calcite-rich fault gouges sheared at sub-seismic sliding velocities, *Pure Appl. Geophys.*, *171*, 2617–2640, doi:10.1007/s00024-013-0760-0.

Viti, C., C. Collettini, and T. Tesei (2014), Pressure solution seams in carbonatic fault rocks: Mineralogy, micro/nanostructures and deformation mechanism, *Contrib. Mineral. Petrol.*, *167*, 970, doi:10.1007/s00410-014-0970-1.

Wang, Q., X. Qiao, Q. Lan, F. Jeffrey, S. Yang, C. Xu, Y. Yang, X. You, K. Tan, and G. Chen (2011), Rupture of deep faults in the 2008 Wenchuan earthquake and uplift of the Longmen Shan, *Nat. Geosci.*, *4*, 634–640.

Wanless, H. R. (1979), Limestone response to stress: Pressure solution and dolomitization, *J. Sediment. Petrol.*, *49*(2), 437–462.

Weeks, J. D., and T. E. Tullis (1985), Frictional sliding of dolomite: A variation in constitutive behavior, *J. Geophys. Res.*, *90*, 7821–7826, doi:10.1029/JB090iB09p07821.

Wong, T.-F., and P. Baud (1999), Mechanical compaction of porous sandstone, *Oil Gas Sci. Tech. Rev. IFP*, *54*(6), 715–727.

Wong, T.-F., and Y. Zhao (1990), Effects of load point velocity on frictional instability behavior, *Tectonophysics*, *175*, 177–195.

Xu, X., X. Wen, G. Yu, G. Chen, Y. Klinger, J. Hubbard, and J. Shaw (2009), Coseismic reverse- and oblique-slip surface faulting generated by the 2008 M_w 7.9, Wenchuan earthquake, China, *Geology*, *37*(6), 515–518.

Yasuhara, H., C. Marone, and D. Elsworth (2005), Fault zone restrengthening and frictional healing: The role of pressure solution, *J. Geophys. Res.*, *110*, B06310, doi:10.1029/2004JB003327.

Zhang, P. (2013), Beware of slowly slipping faults, *Nat. Geosci.*, *6*, 323–324.

Zhang, P., X. Wen, Z. Shen, and J. Chen (2010), Oblique, high-angle, listric reverse faulting and associated development of strain: The Wenchuan earthquake of May 12, 2008, Sichuan, China, *Annu. Rev. Earth Planet. Sci.*, *38*, 353–382.

Zhang, R. Q., Q. J. Wu, Y. H. Li, Z. F. Ding, and R. S. Zeng (2008), Focal depths for moderate-sized aftershocks of the Wenchuan M_s 8.0 earthquake and their implications, *Sci China Ser. D*, *51*(12), 1694–1702, doi:10.1007/s11430-008-0140-2.

Zhang, X., and C. J. Spiers (2005), Effects of phosphate ions on intergranular pressure solution in calcite—An experimental study, *Geochim. Cosmochim. Acta*, *69*(24), 5681–5691.

Zhang, X., C. J. Spiers, and C. J. Peach (2010), Compaction creep of wet granular calcite by pressure solution at 28°C to 150°C, *J. Geophys. Res.*, *115*, B09217, doi:10.1029/2008JB005853.

Zhang, Y., W. Feng, L. Xu, C. Zhou, and Y. Chen (2009), Spatio-temporal rupture process of the 2008 great Wenchuan earthquake, *Sci. China Ser. D*, *52*(2), 145–154.

Zhao, C. P., Z. L. Chen, Q. L. Zhou, Z. X. Li, and Y. Kang (2010), Rupture process of the 8.0 Wenchuan earthquake of Sichuan, China: The segmentation feature [in Chinese with English abstract], *Chin. Sci. Bull.*, *55*(3), 284–292, doi:10.1007/s11434-009-0425-7.